83rd International Scientific Conference of the University of Latvia 2025

GEODYNAMICS AND GEOSPATIAL RESEARCH

CONFERENCE PAPERS

UNIVERSITY OF LATVIA

University of Latvia 83rd International Scientific Conference. Geodynamics and Geospatial Research. Conference Papers. Riga, University of Latvia, 2025, June 12. 64 p.

The conference "Geodynamics and Geospatial Research" organized by the Institute of Geodesy and Geoinformatics of the Faculty of Science and Technology of the University of Latvia addresses a wide range of scientific studies and is focused on the interdisciplinarity, versatility and possibilities of research in this wider context in the future to reach more significant discoveries, including business applications and innovations in solutions for commercial enterprises. The research presented at the conference is at different stages of its development and presents the achievements and the intended future. The publication is intended for researchers, students and research social partners as a source of current information and an invitation to join and support these studies.

Prepared under LU Press
Layout designer: Andra Liepiņa

ISBN 978-9934-36-402-0 (PDF)
https://doi.org/10.22364/iscul.83.ggr.cp

PREFACE

The Institute of Geodesy and Geoinformatics of the University of Latvia (LU GGI) in 2025 celebrates its 101th anniversary.

The researchers of the Institute of Geodesy (1924–1944) concentrated on the research and education in many advanced topics of that time – development and adjustment of National Geodetic networks, photogrammetry, studies of vertical Earth movement and research in gravimetric and magnetic measurements. Currently the research areas are developed in satellite geodesy and geoinformatics. In this context the main topic of LU GGI activities is concentrated on development of satellite laser ranging systems (SLR), both the hardware and control software, two SLR prototypes were developed until 2010 and the new approach – optical space object observation system is developed, and observations is ongoing – latest results were presented at this year's Geodynamics and Geospatial Research.

The light weight and portable digital zenith camera for studies of vertical deflection has been developed at LU GGI. The test results reach precision of 0.1 arc second. This year LU GGI started its project "**Investigation of anomalous refraction effect by using automated digital zenith camera VESTA**", funded by the Latvian Council of Science, project number: lzp-2024/1-0095. The objective of this research work, characterising its novelty, is to explore the behaviour of anomalous refraction (AR) in the Earth's atmosphere by a new approach – using digital zenith camera (DZC) VESTA (VErtical by STArs) and separating AR components from VESTA measurements. AR is the main limiting factor in the accuracy of ground-based astrometric observations causing irregular angular displacements of observed stars.

On July 1st, 2025, new PostDoctoral research project: "**GNSS analytical research competency centre**" will be started at the LU GGI, which tends to strengthen the LU GGI competences in the field of GNSS.

Latest internal restructuring at the University of Latvia has a little bit changed the administrative location of the Institute of Geodesy and Geoinformation and since than LU GGI is the research subunit of the faculty of Science and Technology of the University of Latvia. The Institutes research activities are organized in two research groups – **group for geodynamics and spatial research** led by Dr. sc. ing. **Inese Vārna**, and **group for astrometric observations and research** led by Dr. sc. ing. **Diāna Haritonova**.

The very first conference **Geodynamics and Geospatial Research** was held back in 2017. That time it was pure national conference from year to year it has grown and today we gather speakers and atendees from all around the world. Lessons learnt during worldwide pandemics allows us to welcome speakers from China, USA, Turkey, Ukraine and other countries in the way which is most common for them whether it is on-line or on-site speech.

LU GGI in Latvia is an institution that unites and involves leading researchers from all over the country, regardless of their primal work and has become a sort of informal coordinating centre for research in this field, for example, Geodynamics and Geospatial Research is included in the certification courses list of the Latvian Association of Surveyors thus informing the professionals on the results of the latest research directly. High scientific quality and applied nature of many studies, presented at this conference, will allow to use this knowledge in the economy in the nearest future.

Director of the Institute of Geodesy and Geoinformatics
Dr. sc ing. Ingus Mitrofanovs
June 12, 2025.

TABLE OF CONTENTS

GLOBAL PERSPECTIVES ON THE MAY 2024 GEOMAGNETIC STORM IMPACT ON HIGH-PRECISION POSITIONING BASED ON GEODETIC GNSS OBSERVATIONS

Zhe Yang[1], Jade Morton[2]

[1] *College of Surveying and Geo-Informatics, Tongji University, Shanghai, China*

[2] *Smead Aerospace Engineering Sciences Department, University of Colorado, Boulder, CO, USA*

E-mail: zheyang@tongji.edu.cn

A geomagnetic storm involves a complex interplay between the solar-magnetosphere-ionosphere coupling system and may significantly impact satellite navigation and positioning systems through ionospheric responses. The severity of these storms varies across different events, as the ionospheric electron density fluctuates with different spatial and temporal scales. This study focuses on the geomagnetic storm that occurred on May 10–11, 2024, recognized as one of the most intense storms during the past two decades. Due to its long-lasting effects on both the interplanetary and terrestrial environments, it has gathered considerable attention from both the scientific community and the public sector.

We present a comprehensive analysis of the ionospheric response to the May 2024 storm and its impacts on precise point positioning (PPP) for geodetic GNSS receivers on a global scale. Unlike previous studies, this investigation focuses on the effects on positioning accuracy at the centimeter level, which is an aspect often overlooked in previous research. The results suggest that this storm caused long-lasting and widespread ionospheric disturbances across the North and South American, Asia, Australian, and European sectors. Consequently, high-precision GNSS positioning with a common processing strategy for PPP ambiguity resolution experienced a significant outage. These PPP outages coincided with the growth and decay of the SYM-H index and persisted for over a day at numerous stations located in North America and Australia. This highlights the vulnerability of high-precision positioning applications to the risks imposed by ionospheric disturbances during periods of intense geomagnetic activity.

PREDICTABLE REGULAR DAILY IONOSPHERIC SCINTILLATION

Janis Balodis, Madara Normanda, Ingus Mitrofanovs

University of Latvia, Institute of Geodesy and Geoinformatics, Jelgavas str. 3, Riga, Latvia
E-mail: janis.balodis@lu.lv

The objective of this study is to discover the regular scintillation events as a result of space weather impact on the GPS observation reduction results in Latvian Continuously Operating Reference Stations (CORS) network in selected months in years 2007–2017. In the case of interplanetary Cosmic Ray excess movement in space, the term of the movement of molecular clouds is used [1]. In this study, the term "GPS positioning discrepancy clouds" (clouds) is used when analyzing the nature of the ionospheric scintillation's disturbed positioning results that occurred simultaneously in various number of CORS stations. Union of the subsets of adjacent 90-sec duration clouds is named "wave" where is fixed scintillation simultaneously in 2–3 stations and more. The term "evil waveform" is used to denote the disturbed information for navigation in some area caused by the GPS erroneous information [2]. In this study the regularly daily occurred erroneous waves are searched.

GPS observation data with an elevation cut-off angle of 15° were used for 90 second (sampling data 30 sec) intervals of kinematic post-processing. The FES2004 ocean tidal model was used, along with correction of the solid Earth tide effect. The Dry Global Mapping Function (DRY-GMF) was used for the tropospheric delay modelling. The maximum size of accepted cycle slip corrections was 10. The results of Bernese v5.2 post-processed data of kinematic solution were used.

For further analysis of processing results the authors made software programs were used. Table shows the count of both waves and clouds that should be checked in order to find a regular daily ionospheric impact waves disturbing positioning results.

Table. Monthly ionospheric impact waves and clouds

#	Year	Month	Clouds	Waves	#	Year	Month	Clouds	Waves
1	2007	FEB	1569	120	24	2012	OCT	837	88
2	2007	MAY	4359	308	25	2013	MAY	1587	201
3	2007	JUN	3501	272	26	2013	OCT	3772	152
4	2007	AUG	5830	491	27	2013	NOV	935	114
5	2008	MAR	726	69	28	2013	DEC	1155	136
6	2008	JUN	1600	140	29	2014	FEB	1268	99
7	2008	SEP	1986	193	30	2014	JUN	3393	295
8	2008	OCT	1328	107	31	2014	OCT	1241	117
9	2009	JUL	2473	216	32	2014	DEC	1837	126
10	2009	AUG	1413	126	33	2015	MAR	1584	119
11	2009	OCT	1304	107	34	2015	MAY	1749	170

Table continued

#	Year	Month	Clouds	Waves	#	Year	Month	Clouds	Waves
12	2009	DEC	2056	115	35	2015	JUN	2499	154
13	2010	JAN	255	20	36	2015	OCT	880	118
14	2010	FEB	1123	66	37	2015	DEC	988	119
15	2010	APR	449	59	38	2016	FEB	1166	104
16	2010	NOV	1263	45	39	2016	APR	1401	105
17	2011	MAR	747	48	40	2016	MAY	2541	175
18	2011	AUG	1943	248	41	2016	JUL	3445	339
19	2011	SEP	1477	134	42	2017	APR	1980	120
20	2011	NOV	523	77	43	2017	MAY	2894	136
21	2012	JAN	366	35	44	2017	JUL	6442	214
22	2012	MAR	461	56	45	2017	SEP	1181	126
23	2012	JUL	2155	227	46	2017	OCT	1145	112
		SUM	**38907**	**3279**				45920	3439

The total number of waves is 6718 with a total of 84827 clouds. It is necessary to choose some algorithm to detect the presence of regular waves in these monthly subsets of data. In Figure one of the regular waves in October 13/14, 2013 is described, where in each row description of cloud: No., date, time and list of CORS station DOMEs where positioning discrepancies appeared simultaneously at the same time, is given. Union of the adjacent 90-sec clouds presented as ionospheric scintillation wave's impacted station subset, for simplification also is used to name a wave.

2 2014 OCT 13 23:57: 0 UT LIMB
493 2014 OCT 13 23:58:29 UT OJAR TKMS
494 2014 OCT 14 0: 0: 0 UT TALS MADO SIGU IRBE LUNI LODE MAZS DAGD VANG OJAR ALUK PREI RIGA VAL1 JEK1 LIMB TKMS REZ1 PLSM SALP
495 2014 OCT 14 0: 1:30 UT MADO ALUK DAGD DAU1 BALV BAUS SIGU PREI MAZS PLSM OJAR REZ1 LIMB SALP
496 2014 OCT 14 0: 3: 0 UT DAU1 DAGD PLSM LIMB SALP REZ1 TKMS
497 2014 OCT 14 0: 4:30 UT DAU1 VANG ALUK PLSM LIMB SALP REZ1
498 2014 OCT 14 0: 6: 0 UT REZ1 DAU1 LIMB ALUK
499 2014 OCT 14 0: 7:29 UT DAU1 LIMB
500 2014 OCT 14 0: 9: 0 UT REZ1 LIMB DAU1
501 2014 OCT 14 0:10:30 UT DAU1 RE
502 2014 OCT 14 0:12: 0 UT REZ1 DAU1 TKMS

Fig. Type of regular skewed wave formed by cloud union, with time and peak coverage of clouds (green), beginning of time sequence, median of time sequence and end of time sequence (yellow) and cloud's DOME subsets correspondingly

The search algorithm was developed based on the example of the month of March 2015 [3] where daily regular waves are repeated with a 4.5-minute lag on the time scale, graduated in increments of 90 seconds (1.5 minutes). With the same 4.5-minute step, each of the 1.5-minute clouds shifts from day to day – wave's peak, beginning, median and end (Figure 1). However, the time lag for each of these clouds varies due to the changes of daily wave configuration. The initially assumed 4.5-minute lag also varies and the time scale, graduated in increments of 90 seconds has not been a good fit for regular wave search.

However, the regular wave search was successful. The search difficulties and final results will be presented and discussed in the conference.

The GPS observation reduction results were obtained in 2019–2020 in the Project funded by the Programme for European Cooperating States (PECS), European Space Agency Contract No. 4000128661/19/NL/SC, project "Ionospheric characterization by statistical analysis of Latvian GBAS 11-year selective daily observations". But the current analysis was performed now within the framework of the APC funded by the University of Latvia, Contract No. ZDA 2022/24 as a continuation of analysis of the GNSS data processing results obtained with the Bernese GNSS Software v5.2.

Acknowledgments

The authors would like to express gratitude to Inese Vārna, Diana Haritonova and to Izolde Jumare for their work and assistance in the GNSS data processing with the Bernese GNSS Software v5.2 during (PECS), European Space Agency Contract No: 4000128661/19/NL/SC, project.

References

[1] Baghmanvan, V.; Peron G., et al. *Astrophys*. **2020**, 901, L4. 1–6.

[2] Julien, O., et al. Extension of EWF Threat Model and Associated SOM.

[3] Balodis, J., Normand, M., Zarins, A. R. S. **2023**, 15(8), 2032. 1–21.

GNSS MEASUREMENTS IN HIGH SUN ACTIVITY MALPILS CASE

Jānis Zvirgzds[1], Armands Celms[1], Māris Virkavs[1], Toms Lidumnieks[1, 2], Jolanta Luksa[1], Ivars Bergmanis[1, 2]

[1] *Latvia University of Life Sciences and Technologies, Liela Street 2, Jelgava, Latvia*

[2] *Latvian Geospatial Information Agency, Riga, Latvia*

E-mail: armands.celms@lbtu.lv

GNSS measurements are widely used in determining coordinates and surveying objects in field conditions. It is a fast and effective measuring tool for determining coordinates in open areas. The accuracy and reliability of measurements are influenced by the activity of solar spots. The cycle of solar activity is eleven years and in 2025 activity reaches its peak.

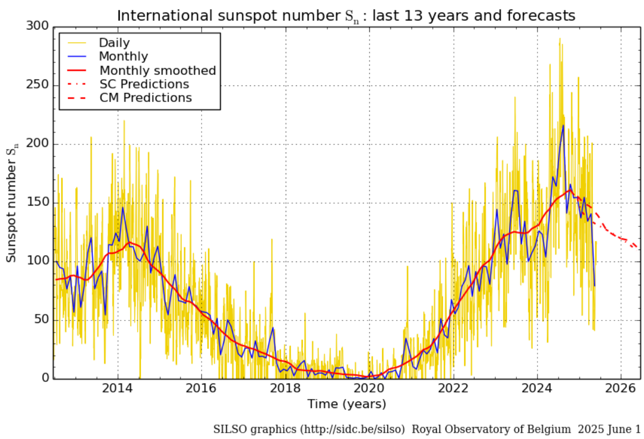

Fig. 1. Source: https://www.sidc.be/SILSO/dayssnplot

On a daily basis, coordinate measurements are carried out by surveyors with instruments from different manufacturers and various types of correction in real-time measurement. The overall goal is to obtain geodetic coordinates within permissible error limits, regardless of the instrument and the time of measurement. To check the operation of GNSS in conditions of high solar activity, the determination of coordinates took place in the middle of the day in good weather. On the day the measurements were taken, the sun's activity significantly increased the number of electrons in the ionosphere.

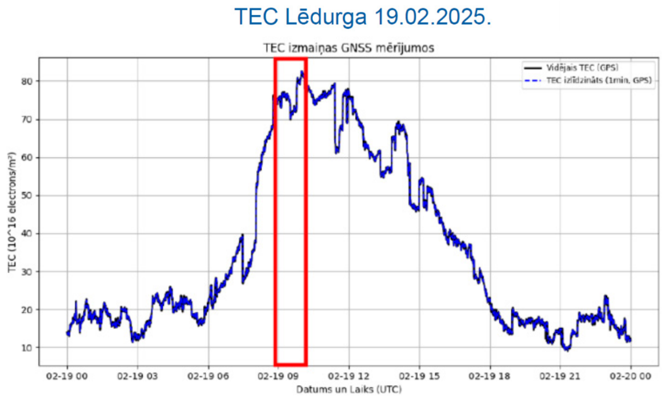

Fig. 2. Source: A. Vallis

The number of electrons in the ionosphere was four times higher than under normal conditions. Two types of coordinate measurement methods were used to detect GNSS malfunctions: stationary measurement with repeated achievement of a fixed position and GNSS measurements on geodetic points located in some locations. The GNSS tools used were with the latest firmware to have the latest coordinate calculation methods. Measurements were also made with a GNSS RTK instrument that is at least 10 years old.

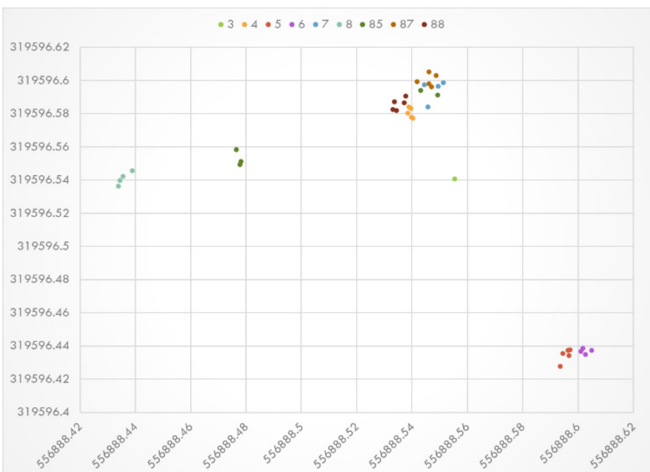

Fig. 3. Results of divergent fixations of different corrections

A statistical examination of the obtained data and grouping by type of correction demonstrates that the difference in fixed coordinates exceeds both the values given by the manufacturer and the accuracy to be achieved in regulatory enactments.

Conclusions

When analysing the data, no regularities were found when performing repeated measurements. This proves that solar activity and Total Electron Content affect GNSS measurement results and reduce their reliability.

Keywords: GNSS; GNSS accuracy; Real Time Kinematic (RTK); Radio modules; Global position measurements.

IONOSPHERIC ACTIVITY STUDIES IN THE TERRITORY OF LATVIA USING RINEX BASE STATION DATA

Atis Vallis

Lejaslīves SIA., Lejaslīves, Krimulda par., Sigulda distr., LV-2144, Latvia
E-mail: info@lejaslives.lv

1. Purpose

The purpose of this study is to develop a computer algorithm that would independently analyze and graphically display GNSS post-processing data from the LatPos network's Continuously Operating Reference Stations (CORS) in Latvia in order to obtain information about ionospheric activity.

The output of the algorithm, specifically the obtained information about ionospheric activity, will help increase work productivity and assist users when GNSS data is partially missing. It will support Global Navigation Satellite System (GNSS) Real-Time Kinematic (RTK) measurements by providing visually interpretable graphs that reflect Total Electron Content (TEC) fluctuations and their effect on the accuracy of GNSS observations [2, 4, 7, 8, 9, 10].

Provision of visually perceptible graphs that reflect Total Electron Content (TEC) fluctuations and their impact on the accuracy of GNSS measurements will help users of Global Navigation Satellite System's (GNSS) Real Time Kinematics (RTK) survey methods to increase work productivity and provide with missing information [2, 4, 7, 8, 9, 10].

2. Test data

The test data used in this study are RINEX (Receiver Independent Exchange) files from the LatPos GNSS reference station network. These files contain GNSS satellite signal observations, such as L1 and L2 carrier frequencies, C/A and L2C (M) code pseudorange data, as well as signal recording timestamps.

Only NAVSTAR (U.S. – Navigation System with Timing And Ranging) GPS (Global Positioning System) data obtained from this network were used in this work. The data processing, including extraction and calculation of relevant parameters, was carried out using the Python programming environment [5, 12].

3. Theoretical basis

TEC is the total number of electrons in the upper layers of the ionosphere (between the GNSS satellite and the receiver), which affects (most often hinders) the propagation and accuracy of GNSS signals. TEC calculations are used based on pseudorange and carrier phase differences for NAVSTAR satellites at two carriers L1 and L2 [3, 6, 9].

$$TEC = \int_{receiver}^{satellite} N \cdot ds \tag{1}$$

Each satellite transmits two carrier signals in the form of electromagnetic waves at the following carrier frequencies L1 = f_1 = 1575.42 MHz with a wavelength λ_1 = 19 cm and L2 = f_2 = 1227.60 MHz with a wavelength λ_2 = 24 cm.

4. TEC Calculation from GPS Observations

Pseudodistances obtained from the code (C/A, L2C (M)) travel time [2, 4, 7].

$$P = \rho + c \cdot (dT - dt) + \Delta i_i^{iono} + \Delta^{tropo} + b_i^{P,r} + b_i^{P,s} + m_i^P + \varepsilon_i^P \tag{2}$$

Where:

i = 1, 2 corresponding to Pseudodistances P_1 (C/A) and P_2 (L2C (M))

P – is the code pseudorange measurement (in distance units)

ρ – is the geometrical range between satellite and receiver

c – is speed of light in vacuum

dT – is satellite clock offset from GPS time

dt – is receiver clock offset from GPS time

$\Delta i_i^{iono} = \frac{(40.3 \cdot TEC)}{f_i^2}$ ionospheric delay

f_i – is the carrier frequency Li

Δ^{tropo} – tropospheric delay

$b_i^{P,r}$ – are the receiver instrumental delays on P

$b_i^{P,s}$ – are the satellite instrumental delays on P

m_i^P – multipath effect on P

ε_i^P – receiver noise on P

Carrier phase observations are obtained from the carrier signal travel time [2, 4, 7, 9, 11].

$$\Phi_i = \lambda_i \cdot \phi_i = \rho + c \cdot (dT - dt) + \lambda_i + N_i - \Delta i_i^{iono} + \Delta^{tropo} + b_i^{\phi,r} + b_i^{\phi,s} + m_i^{\phi} + \varepsilon_i^{\phi} \tag{3}$$

Where:

Φ_i – are carrier phase observation (in distance units)

ϕ_i – are carrier phase observation (in cycles)

$\lambda = c/f$ is the wavelength

N_i – are the unknown number of Li integer carrier phase ambiguities

$b_i^{\phi,r}$ – are the receiver instrumental delays on

$b_i^{\phi,s}$ – are the satellite instrumental delays on

m_i^{ϕ} – multipath effect on

ε_i^{ϕ} – receiver noise on

This formula describes the GPS pseudorange (P and) measurement, including various factors that affect the signal path and time measurements.

TEC is the number of free electrons per square meter along the path of an electromagnetic wave traveling between a GPS satellite and a ground-based receiver. It is an important parameter in ionospheric studies and navigation corrections.

TEC is typically measured using GPS signals by analyzing the differences in pseudorange and carrier phase measurements between the two main GPS frequencies – L1 and L2.

Subtracting pseudorange measurements for L1 and L2 frequencies:

$$P_2 - P_1 = 40.3 \cdot TEC\ (1/f_2{}^2 - 1/f_1{}^2) \tag{4}$$

By rearranging this expression, TEC can be expressed as:

$$TEC = \frac{(P_2 - P_1)}{40.3 \cdot (1/f_2{}^2 - 1/f_1{}^2)} \tag{5}$$

When calculating a denominator containing known numerical values:

$$40.3 \cdot (1/f_2{}^2 - 1/f_1{}^2) = 1.05046 \times 10^{-5}$$

TEC simplifies to:

$$\mathrm{TEC} = (P_2 - P_1) \cdot 95215 \tag{6}$$

where 95215 is the scaling factor in TEC electrons/m^2.

TEC can be alternatively expressed as Total Electron Content Units (TECU). TECU is TEC expressed as 10^{16} electrons/m^2.

$$TEC\ (TECU) = (P_2 - P_1) \cdot 9.52 \tag{7}$$

This value is widely used in scientific literature [15, 16].

GPS pseudorange and carrier phase measurements can be used to calculate TEC in the ionosphere. If TEC is expressed in electrons/m^2, the factor 95215 is used, and if TEC is expressed in TECU units, the factor 9.52 is used.

TEC calculation based on pseudoranges (TEC P) and carrier phase differences (TEC Φ) is described below.

Combining the pseudorange observations *P*, we obtain the TEC value [2, 6, 10, 14]:

$$TEC\ P = 9.52 \cdot (P_2 - P_1) + various\ errors \tag{9}$$

In turn, combining the carrier phase observations, we obtain:

$$TEC\ \Phi = 9.52 \cdot (\Phi_1 - \Phi_2) - (N_1\lambda_1 - N_2\lambda_2) + various\ errors \tag{10}$$

Calculating the difference between these two quantities resolves the uncertainty.

$$TEC\ L = TEC\ \Phi - (TEC\ \Phi - TEC\ P) \tag{11}$$

TEC is essential in geophysics and has applications in navigation measurement corrections for single-frequency receivers, as there is no way to calculate this uncertainty.

Traditionally, TEC was measured using the Faraday rotation effect on a linearly polarized plane wave.

5. Development progress

Python Software version 3.13.1 with georinex, numpy, pandas, matplotlib, gzip and other libraries were used to automate the calculations.

In order to test the operation of the algorithm time effectively, a 10-minute RINEX file was created.

Figure 1. displays test data analysis for a 10-minute RINEX file on 23.01.2025 LGIA (Latvian Geospatial Information Agency).

6. Results

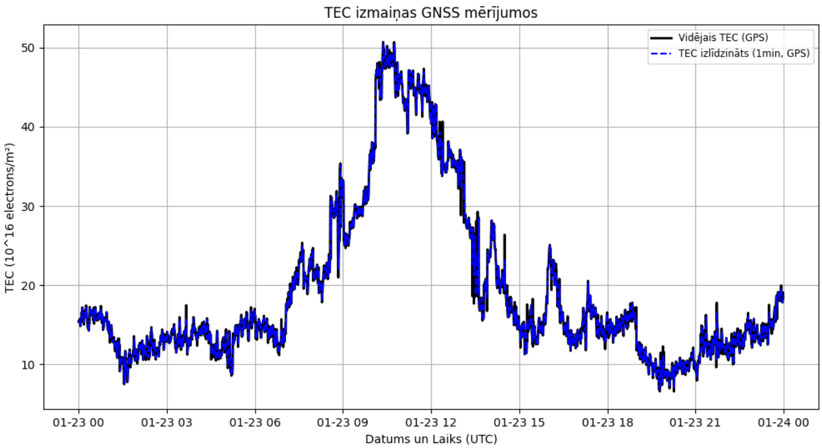

Fig. Test data TEC graph of 23.01.2025

References

[1] Leick, A. *GPS satellite surveying* (2nd ed.). John Wiley & Sons, Inc. **1995**.

[2] Klobuchar, J. A. Ionospheric total electron content (TEC). In *Handbook of Geophysics and the Space Environment*. **1985**.

[3] Hoffmann-Wellenhof, B.; Lichtenegger, H., & Collins, J. *GPS theory and practice*. Springer-Verlag Wien. **1994**.

[4] Komjathy, A. *Global ionospheric total electron content mapping using the Global Positioning System* (Doctoral dissertation). **1997**.

[5] Gail, W. B.; Prag, B.; Coco, D. S., & Cooker, C. A statistical characterization of local mid-latitude total electron content. *Journal of Geophysical Research*. **1993**, *98*(A9), 15,717–15,727.

[6] Seeber, G. *Satellite geodesy*. Walter de Gruyter. **1993**.

[7] Komjathy, A., & Langley, R. B. *An assessment of predicted and measured ionospheric total electron content using a regional GPS network*. **1996**. Retrieved from http://gauss.gge.unb.ca/grads/attila/papers/papers.htm (accessed 17 September 1998).

[8] Lanyi, G. E., & Roth, T. A comparison of mapped and measured total ionospheric electron content using global positioning system and beacon satellite observations. *Radio Science*. **1988**, *23*, 483–492.

[9] Mannucci, A. J.; Wilson, B. D., & Edwards, C. D. A new method for monitoring the Earth's ionospheric total electron content using GPS global network. In *Proceedings of ION GPS-93*, Salt Lake City, UT, 22–24 September, The Institute of Navigation, Alexandria, VA. **1993**, 1323–1332.

[10] Sardon, E.; Rius, A., & Zarraoa, N. Estimation of the transmitter and receiver differential biases and the ionospheric total electron content from global positioning system observations. *Radio Science*. **1994**, *29*, 577–586.

[11] Klobuchar, J. A. Ionospheric effects on GPS. In B. W. Parkinson & J. J. Spilker (Eds.), *Global Positioning System: Theory and Applications*. **1996**, *1*, 370. American Institute of Aeronautics and Astronautics.

[12] Wilson, B. D., & Mannucci, A. J. Instrumental biases in ionospheric measurements derived from GPS data. In *Proceedings of ION GPS-93*, Salt Lake City, UT, 22–24 September, The Institute of Navigation, Alexandria, VA. **1993**, 1343–1351.

[13] Kantor, I. J.; de Paula, E. R., & de Rezende, L. F. C. (nd). TEC measurements with GPS data. INPE, Aeronomy Division, São José dos Campos, São Paulo – Brasil.

[14] Difar, K. A. *Studying the relationship between TEC, I95 index and Wp index and their effect on ionosphere in Iraq, Romania and South Africa*. Polytechnic University of Bucharest, Romania. **2019**.

[15] Choi, B.-K., et al. Receiver DCB Estimation and Analysis by Types of GPS Receiver. *Journal of Astronomy and Space Sciences*. **2010**, *27*(2), 123–128.

[16] NOAA Space Weather Prediction Center. Total Electron Content. https://www.swpc.noaa.gov/phenomena/total-electron-content.

RIGA SATELLITE LASER RANGING STATION: 2024 OVERVIEW

Kalvis Salmins, Jorge del Pino[†], Janis Kaulins, Stanislav Melkov

University of Latvia, Institute of Astronomy Jelgavas str. 3, Riga, Latvia
E-mail: kalvis.salmins@lu.lv

This paper outlines the operational status and key developments at the Satellite Laser Ranging (SLR) Station 1884 Riga during the year 2024. The station's activities are structured around three key areas: system modernisation, routine satellite laser ranging operations, and research and development initiatives in support of space situational awareness.

In October 2024, significant meteorological instrumentation upgrades were implemented. These included the installation of a Vaisala WXT-56 automatic weather transmitter as replacement for the old WXT-512 model, a PACE 1000 absolute barometer, a soil moisture sensor, and a new groundwater level measurement device.

System modernisation efforts focused on expanding the station's capabilities to include satellite photometry and bistatic laser ranging. Bistatic space debris observation campaigns were conducted in collaboration with the Graz and Borowiec SLR stations, both equipped with high-intensity lasers. Furthermore, the Riga station participated in a photometric observation campaign of the rocket body 87074G and the defunct satellite 82092A.

Performance metrics and contributions to the International Laser Ranging Service (ILRS) network will be presented, highlighting main achievements and possible improvements.

RECENT RESULTS OF POSITIONAL ASTROMETRIC OBSERVATIONS AT THE GGI

Diana Haritonova, Ansis Zarins

University of Latvia, Institute of Geodesy and Geoinformatics, Jelgavas str. 3, Riga, Latvia
E-mail: diana.haritonova@lu.lv

We propose the method of CCD frame stacking, which is implemented in equatorial coordinates, thus having several advantages in searching space objects using passive optical systems. This method enables increasing the efficiency of capturing faint space objects also in imperfect observation conditions and at different locations.

The proposed method allows to prolong the "effective exposure time" of near-Earth objects (NEOs), and it can be realized using CCD frames obtained at different epochs and via several optical systems simultaneously. The method enables increasing the brightness of GEO (geostationary orbit) and LEO (low Earth orbit) debris or visualizing their motion relative to stars.

As space debris and NEO observation communities use similar technology (telescopes, radar systems, instrumentation) and processes to measure space objects (observation techniques, data processing approaches), the need for synergy is growing.

The Institute of Geodesy and Geoinformatics (GGI) of the University of Latvia is focused on positional astrometric observations of different space objects by the optical tracking system (OTS) using a control and data processing software, which is developed at the institute. The OTS includes twin receiving optical tube assemblies, which are symmetrically mounted on an Alt-Alt mount. Two CCD matrices are used for observation purposes, the more advanced one is 16.8 Mpix CCD matrix, ensuring a field of view of 0.5° × 0.5°. The software package is capable of automatic near-real-time processing of CCD frames, star identification and astrometric position determination of space objects.

In this study, recent observation results obtained by the OTS are summarized and compared, showing the efficiency of the proposed method of frame stacking.

Acknowledgements

The research is financed by the Recovery and Resilience Facility project "Internal and External Consolidation of the University of Latvia", No. 5.2.1.1.i.0/2/24/I/CFLA/007.

Valuable support was given by MikroTik and the University of Latvia Foundation in the procurement of a new CCD matrix and focuser. Project No. 2283.

TERRESTRIAL GRAVIMETRIC GEOID MODEL DEVELOPMENT IN LATVIA

Vents Zusevics

Latvian Geospatial information agency, O.Vaciesa 43, Riga, Latvia
E-mail: vents.zusevics@lgia.gov.lv

Global positioning methods are the basis of modern infrastructure. For practical application of global positioning, it is crucial to precisely transform the observed ellipsoidal heights to national height reference frame. The modelling of such transformation surfaces, also called gravimetric quasigeoids, is done, fitting gravimetric geoids to the chosen height reference frame. The most important input of said gravimetric geoids can be assumed to be pointwise gravity data.

Historically, gravity data coverage in Latvia has developed sporadically, within campaign efforts spanning multiple years. Between such campaigns there can be seen significant differences in instruments, field and post-processing workflows used, and final value accuracy estimations. Gravity surveys in Latvia pre-2022 have been done with final data density ranging from 1.5 km in central areas up to 15 km in eastern parts of the country. Geoid models traditionally are calculated, using interpolation methods powered by input data set statistics. Variations in data precision and density negatively influence accuracy, robustness and error evaluation of resulting models. When performing unification of data sets of varying origins and accuracy, intercomparison and harmonization is a must; for this, statistically significant overlaps in information must be provided.

Over a new gravity survey, between 2022 and 2025, 2658 new pointwise gravity values have been obtained. Data provides 4 km data step over the eastern part of Latvia. New data is validated by independent repeat measurements. Precision evaluation is presented, based on validation and post processing results. Validation of pre-2022 data has been used for older data error evaluation. Both new and old data have been harmonized and included in the new gravity reference frame LAG-2019.

Free air anomaly grids were calculated and used in old and new data comparison. Comparison results reflect the positive influence new data will have on a new gravimetric geoid development in Latvia.

GNSS LEVELLING FOR 1ST CLASS LEVELLING NETWORK – A SECOND LOOK

Łukasz Borowski[1], Piotr Banasik[2], Kamil Maciuk[2]

[1] *Faculty of Social Sciences, University of the National Education Commission, Krakow, 2 Podchorążych St., 30–084 Krakow, Poland*

[2] *Department of Integrated Geodesy and Cartography, AGH University of Krakow, 30 Mickiewicz Av, 30–059 Krakow, Poland*

E-mail: lukasz.borowski@uken.krakow.pl

The presentation is the authors' second look at an adaptation of GNSS-levelling for establishing a national vertical network in Poland. The previous one was presented at last year's Geodynamics and Geospatial Research 2024. The new presentation results from the authors' reflections, primarily in balancing cost/quality (accuracy) effects. The reason for this consideration is the decision of the Polish Head Office of Geodesy and Cartography (HOGC) to commission new measurements for the basic vertical network (average accuracy not exceeding 1.5 mm/km). The first after the PL-EVRF2007-NH frame was adopted, in the HOGC and 380 powiat's geodetic data sets [1, 2]. It is visible that some powiats (second level of the Polish administrative division) remain without national vertical network benchmarks (Fig.). Therefore, establishing their own (detailed class, 4 mm/km) network is limited, as the height component of the datum cannot be transferred via short-range levelling sections. The solution is to commission (by powiat) some levelling works outside their administrative area (in practice: not allowed or limited acceptability) or to establish some points by GNSS levelling as a reference for the detailed levelling. HOGC considered the second solution a potentially efficient method, due to its relatively low cost, and the possibility of passing terrain obstacles [3]. So far, it hasn't been used in Poland for such works, and because of that, the measurement standard hasn't been adopted. Therefore, an analysis and measurement experiment was commissioned for four independent research teams in 2023. We are the authors of one of those analyses, and present its final results – standard recommendation, recently published [4]. Overall, the defined GNSS-levelling method shows potential as a cost-effective approach for extending the Polish 1st-class vertical control network.

Method of the experiment – height differences between 7 first-class geodetic network points (including 2 ASG-EUPOS stations' auxiliary points) were measured (vectors: 15–31 km) using typical surveying equipment to reflect the accuracy achievable by an average surveying company. SatLab Freya receivers and Trimble Business Centre 5 software were used, without high-end tools like individual antenna calibrations or Bernese GPS Software. Observations were performed over two days, with 12-hour sessions and a 5° elevation mask. Normal height differences were calculated using the PL-geoid2021 model. The data was analysed for session lengths of 2, 4, 6, 8, and 12 hours, and four satellite systems configurations. Two vector calculation methods were used: single vector solution (similar to geometric levelling) and each-to-each (connecting all points). A total of 40 scenarios were analysed.

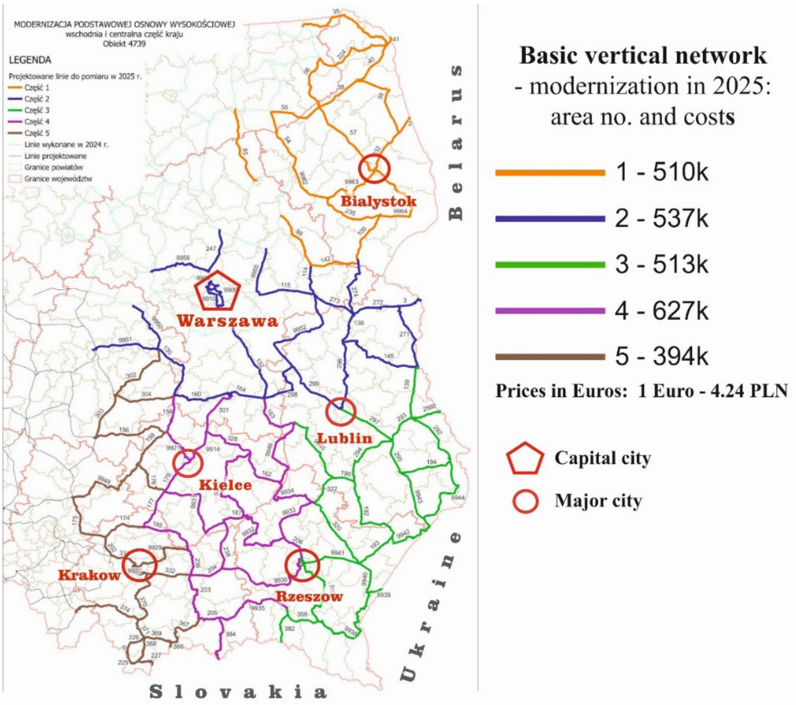

Fig. Polish vertical network – a newly commissioned geometric levelling works: parts and their costs, figure and data based on [5]

References

[1] Borowski, Ł.; Kubicki, B., & Gołąb, J. Implementation of the EVRF2007 height reference frame in Poland. *Journal of Applied Geodesy*. **2023**, *17*(4), 313–323. https://doi.org/10.1515/jag-2023-0020.

[2] Borowski, L., & Banasik, P. The conversion of heights of the benchmarks of the detailed vertical reference network into the PL-EVRF2007-NH frame. *Reports on Geodesy and Geoinformatics*. **2020**, *109*(1), 1–7. https://doi.org/10.2478/rgg-2020-0001.

[3] Banasik, P., & Bujakowski, K. The Use of Quasigeoid in Leveling Through Terrain Obstacles. *Reports on Geodesy and Geoinformatics*. **2017**, *104*(1), 57–64. https://doi.org/10.1515/rgg-2017-0015.

[4] Borowski, Ł., Banasik, P., & Maciuk, K. Application of GNSS-levelling for updating the base vertical network. *Journal of Applied Geodesy*. **2025**, https://doi.org/10.1515/jag-2024-0096.

[5] Geoforum.pl. **2025**, May 12. *GUGiK przeznaczy prawie 13 mln zł na modernizację osnowy wysokościowej*. https://geoforum.pl/index_print.php?option=print&table=news&name=35973_GUGiK_przeznaczy_prawie_13_mln_zl_na_modernizacje_osnowy_wysokosciowej.

COMPUTATION OF THE IGS20 COORDINATES FOR ROMPOS NETWORK

Vlad Sorta, Mihaela Simina Puia, Miluță Flueraș

National Center for Cartography, Expozitiei no. 1A, Bucharest, Romania
E-mail: vlad.sorta@cartografie.ro

The development of GNSS reference networks at national and regional level has led to the need to integrate them into European and international networks. This involves the coordinate computation of GNSS antennas for the reference stations, both in ETRF and ITRF/IGS systems, ensuring a high precision and accuracy. This task can only be achieved by performing a rigorous data analysis using scientific software, designed for this purpose.

The presentation approach the coordinate computation of ROMPOS GNSS reference stations in IGS20 reference frame, according to the EPN Guidelines.

The Romanian Position Determination System – ROMPOS was officially launched in September 2008, having at that time a network of 48 GNSS reference stations as basic infrastructure. These were uniformly distributed throughout the national territory [5].

Over the years, the National Network of Permanent GNSS Stations has undergone a continuous process of modernization and expansion. Today it consists of 86 GNSS reference stations, covering the whole territory of Romania and, in addition, 20 more stations operated by neighbouring countries in the border area, namely Hungary, Ukraine, the Republic of Moldova and Bulgaria (countries with which cross – border GNSS data exchange agreements have been concluded). The Agreement with Serbia is being ratified also. The current configuration of the ROMPOS network is shown in the Figure.

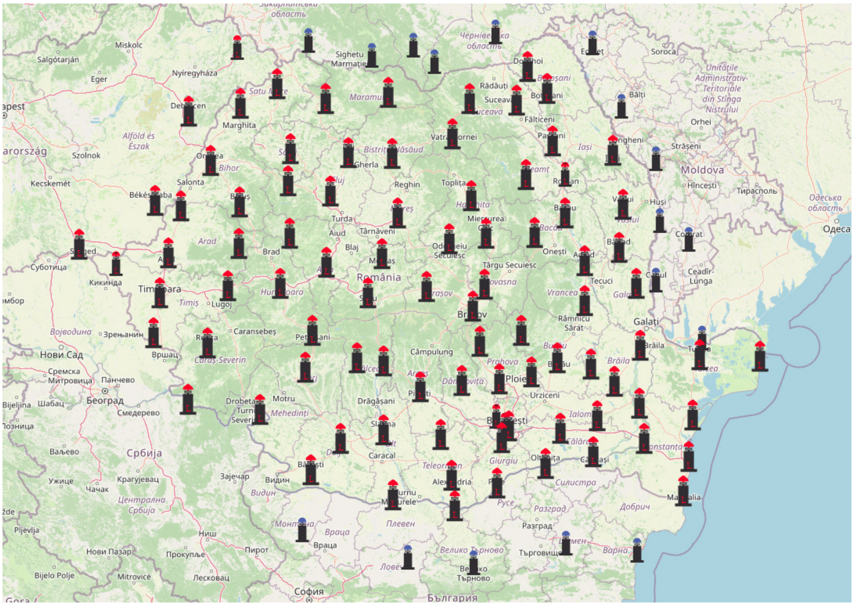

Fig. Current ROMPOS network configuration [5]

The general purpose of reprocessing of the whole National GNSS Network in the IGS20 reference frame is to increase the quality of the physical coordinates of the GNSS antennas [3] and, on the other hand, to complete the process of integrating the National GNSS Network into the European EUREF-EPN network [4], by approving the documentation regarding reprocessing it in a scientific approach, according to their Guidelines [2].

It has to be mentioned that, for those who are new to the EPN processing Guidelines and new to the Bernese GNSS Software 5.4 version (BSW 5.4) [1], EPN has set up a so called benchmark campaign, in order to help ACs to make sure that the processing chain they set up is fine and in full agreement with the Guidelines. The involved data stems from 40 GNSS reference stations, covering most of the cases which can occur in the networks.

By processing the datasets related to the year 2023 – 7 days (GPS week 2293) with BSW V.5.4, running the specific programs were obtained the coordinates in IGS20 system, at the 2015.01.01 00:00:00 reference epoch, according to EPN Guidelines, which were briefly described in the current subsection. It has to be mentioned that, the data processing has been run both manually and automatic, using the BPE (Bernese Processing Engine), specifically the Process Control File RNX2SNX.PCF.

The correctness of the results and the software configuration were checked and confirmed by Analysis Coordinator of the EPN, based on the benchmark campaign. This allowed the transition to the next stage, namely that of testing the processing including data from the ROMPOS network, for a 15 days interval, between 19.07.2024 and 08.08.2024 (GPS days 207–221).

After the initial verification of the results by the EUREF Governing Board specialist, it were obtained very good values of mean repeatability, namely 0.85, 0.72, and 2.75 (NEU, respectively, in mm).

References

[1] Dach, R.; Fridez, P. *Bernese GNSS Software Version 5.4* – Tutorial.

[2] Kenyeres, A.; Bellet, J. G.; Bruyninx, C.; Caporali, A.; de Doncker, F.; Droscak, B.; Duret, A.; Franke, P.; Georgiev, I.; Bingley, R.; Huisman, L.; Jivall, L.; Khoda, O.; Kollo, K.; Kurt, A. I.; Magyar, B.; Mesmaker, D.; Morozova, K.; Nágl, J.; Özdemir, S.; Papanikolaou, X.; Parseliunas, E.; Stangl., G.; Ryczywolski, M.; Tangen, O. B.; Valdes, M.; Zurutuza, J.; Weber, M. Regional integration of long-term national dense GNSS network solutions. *GPS Solut*. **2019**, *23*, 122.

[3] Kenyeres, A. *Categorization of permanent GNSS reference stations*. https://www.epncb.oma.be.

[4] https://www.epncb.oma.be/_productsservices/coordinates/ (Legrand J. (**2022**): EPN multi-year position and velocity solution CWWWW, Available from Royal Observatory of Belgium, https://doi.org/10.24414/ROB-EUREF-CWWWW).

[5] https://rompos.ro/Informații_tehnice.

PRELIMINARY RESULTS FROM REASSESSMENT OF THE RECENT VERTICAL MOVEMENTS OF THE EARTH'S CRUST IN BULGARIA

Vasil Cvetkov, Christina Mickrenska

University of Architecture, Civil Engineering and Geodesy, Hristo Smirnenski Blvd. 1, Sofia, Bulgaria
E-mail: tzvetkov_vasil@abv.bg

Several maps depict the recent vertical movements of the Earth's crust in Bulgaria's territory [1, 2, 3, 4]. According to Kanev and Mladenovski [2], almost the whole territory of Bulgaria is rising. The magnitude of the uplifts is mainly 1–2 mm/y. The supreme uplift velocities, with values exceeding 4 mm/y, are in the Pirin mountain and the Kotel-Omurtag part of the Balkan /Stara Planina/. The sinking areas are the South-Middle Rhodopes and the Strandja–Sakar mountains, where the drop speeds of the Earth's crust are up to –3 mm/y. The standard errors of the estimated vertical velocities are not given in the publication [2].

Contrary to Kanev and Mladenovski, Gospodinov et al. [3] estimate that the whole territory of Bulgaria is sinking. According to the authors, the values of the velocities are mainly in the range –1 ÷ –2 mm/y. The maximum fall of –3.4 mm/year is in the Lom depression, located in the southwest part of the Moesian Platform. The standard errors of the determined velocities are 0.7 mm/year on average.

A different picture of the tectonic motions in the territory of Bulgaria is presented by Belyashki [1]. According to [1], the velocities are predominantly in the range from 0 to –2 mm/y. The velocities between –2 mm/year and –3.5 mm/year are in the Lom depression and the Western Forebalkan. The mountains Pirin, Rila, and Central Rhodopes are rising by 1–2 mm/y. A similar rise is also detected in the Lodugorie-Dobrudzha Swell and the Strandzha mountain. The standard errors of the obtained velocities vary from 0.1 mm/year in Eastern Bulgaria to 1 mm/year in Western Bulgaria.

Another estimation of the recent vertical movements of the Earth's crust in Bulgaria is given by Spiridonov and Georgiev in their study [4]. According to the authors, the Lom depression is sinking by –2.5 mm/year. The central area of the Bulgarian Moesian Plain is rising by approximately 1 mm per year. The Western Forebalkan and the Balkan are sinking approximately –1 mm/year, but the Central Balkan is rising by 2 mm/year. The rates of rise for the Rila, Pirin, Rhodopes, and Sakar are 2 mm/year, 4 mm/year, 3.5 mm/year, and 1.5 mm/year, respectively. The authors did not give standard errors of the mentioned vertical velocities. As they remarked, there is no geomorphological logic between the presented vertical velocities and the known active faults in the territory of Bulgaria. Moreover, the South-Moesian fault [7, 8] is not detected in their investigation.

What is in common between the discussed vertical velocities in the studies [1, 2, 3, 4] is:

- They are based on the adjustments of the precise levelling data from three different epochs. In the study [2], the data from the First and the Second Levelling of Bulgaria were used. In the studies [1, 3], the data from the First and the Third Levelling of Bulgaria were used. In the study [4], all available levelling data were analysed.

- The adjustments of the levelling networks used the mean of both measurements of line elevations, which is the supreme systematic error considering levelling data processing [5].
- The adjustments were performed without minimising the standard errors of the adjusted benchmark heights [6].

As a result, using the same data, different results were obtained, and these results do not correspond with the active tectonic faults in Bulgaria [4, 7, 8].

To yield independent results considering the recent vertical movements of the Earth's crust in Bulgaria, we applied a different estimation approach.

We used the data from the Second and Third Levelling of Bulgaria. We applied 3^n independent adjustments of both networks to select those measured line elevations that minimise the loop errors in the networks [5]. We also applied Inverse Distance Weighting iterative adjustments [6] with a power parameter equal to 6. As a result, the standard errors of the adjusted benchmark heights in both networks, those of the Second Levelling /1953–1957/ and the First Phase of the Third Levelling /1975–1980/, are between 2 mm and 4 mm. Thus, the standard errors of the vertical velocities are on average 0.17 mm/year. The recalculated vertical velocities are shown in Fig.

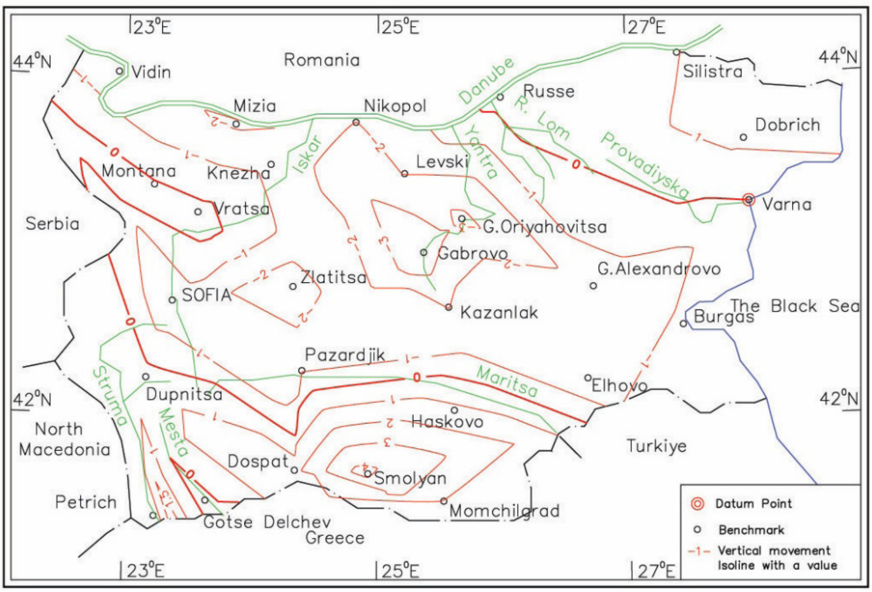

Fig. The new map of the recent vertical movements of the Earth's crust in Bulgaria

According to Fig. 1, the territory of Bulgaria, considering the signs of the yielded vertical velocities of the Earth's crust, can be divided into five parts.

The first one is the Eastern part of the Lodugorie-Dobrudzha Swell. This part of Bulgaria is rising by 1 mm/year. The boundary, that is to say, the velocity zero line, starts from the Varna Bay, passes along the rivers Pomoriyska, Beli Lom and Rusenski Lom. Thus, this zero line is very close to the Intramoesian Fault sketched by Fig. 2 in [8] and coincides with a group of active faults given in this sketch.

The second part includes the rest of the Moesian Platform, the Forebalkan, the part of the Balkan located East of the Iskar River, the Tracian Plain, and the Strandzha-Sakar massifs. All this territory is sinking by 1–2 mm/year. The only exception is the area along the Yantra river between the towns of Gabrovo and Gorna Oriyahovitsa, where the velocities of sinking are up to –3.5 mm/year. This sinking is likely a logical result of the intensive seismic activities in this place [8, Fig. 11]. Our results confirm the sinking of the Lom depression by 1.5–2.5 mm/year.

The south boundary of the second part is the Maritsa fault, extending between the mountains Vitosha and Rila, following the boundary between the Kraishte and Sredna Gora, according to Gabarov's geomorphological zonation of Bulgaria [7, Fig. 2]. South of this line, which is an agglomerate of important neotectonic faults [7, Fig. 7], is located the third tectonic part in Bulgaria, which is rising by 1–2 mm/year. The supreme rise of +4.3 mm/year we registered in the area of Smolyan town, which is close to the highest Rhodopes' peak – Golyam Perelik. Other rises more significant than 3 mm/year we yielded in Madan / 3.5 mm/year /, and Zlatograd / 3.2 mm/year /. Considering the Pirin Mountain, we found that the territory of Papas Chayr passage is rising by 1.7 mm/year. The area of Kroupnik town, which is famous for extensive seismic activity, is rising by 1.4 mm/year.

The only zone south of the Maritsa fault and its extension between the Kraishte and Sredna Gora [7, Fig. 7], where we registered sinking, is the area of the Mesta River fault. According to our calculations, the area around Gotse Delchev is sinking by 0.5 mm/year.

The last fifth zone is the Western part of the Stara Planina, located west of the Iskar River. This zone is surrounded by the Forebalkan fault in the North [8, Fig. 2], the Iskar River fault in the East, and the boundary between the Forebalkan and the Stara Planina in the South [7, Fig. 4, Fig. 8]. The registered rise between Belogradchik and the Prevala passage is approximately 0.8 mm/year, which is higher than the standard errors of the velocity multiplied by three.

In conclusion, we can say that the velocities of the vertical movements of the Earth's crust in Bulgaria are between ±2 mm/year, except for the area of the Yantra River gouge meanders and the peak of Golyam Perelik. All boundaries between the zones with positive and negative velocities follow well-known active faults.

Acknowledgements

The authors express gratitude to the Centre for Scientific Research and Design at the UACEG for funding and support for the completed research project under contract No BN315/2025 on the topic "Optimisation of levelling networks by studying the applicability of resampling methods."

References

[1] Belyashki, T. A new map of the recent vertical movements of the Earth's crust on the territory of Bulgaria. *Geodezia, kartographia, zemeustroistvo.* **2012**, *3–4*, 3–5 (in Bulgarian).

[2] Kanev, D.; Mladenovski, M. The recent vertical movements of the Earth's crust in Bulgaria. *Journal of the Bulgarian Geographical Society.* **1969**, *IX*, 17–26 (in Bulgarian).

[3] Gospodinov S.; Peneva E.; P. Penev. A specific approach to least squares adjustment of the state levelling network, *Proceedings of the 22nd International Multidisciplinary Scientific GeoConference SGEM 2022*, Albena, Bulgaria. **2020**, *22*(2.1). Publisher: STEF92 Technology. https:/doi.org/10.5593/sgem2022/2.1/s09.20.

[4] Spiridonov H.; Georgiev N. Study of the Neotectonics and Geodynamics of the Republic of Bulgaria, *Aerospace Research in Bulgaria*, **2003**, *17,* 84–96.

[5] Cvetkov, V. On initial data in adjustments of the geometric levelling networks (on the mean of paired observations). *Journal of Geodetic Science*, **2024**, *14*(1), 20220170. https://doi.org/10.1515/jogs-2022-0170.

[6] Cvetkov, V.; Gospodinov, S. Inverse Absolute Height Weighting in the Highest Order Levelling Networks, *EGU General Assembly 2023*, Vienna, Austria, 24–28 Apr **2023**, EGU23-4219. https://doi.org/10.5194/egusphere-egu23-4219.

[7] Zagorchev, I. Geomorphological zonation of Bulgaria. Principles and state of the art, *Proceedings of the Bulgarian Academy of Sciences*, **2009**, *628*(8), 981–992.

[8] Stanciu, I.; Ioane, D. Geomorphological and Neotectonic Structures Studied in the Southern Part of the Moesian Platform in Romania. *Geographies* **2023**, *3*, 743–762. https://doi.org/10.3390/geographies3040040.

UNCERTAINTY OF A STATE VERTICAL REFERENCE SYSTEM BELOW 1 MGPU – IS IT POSSIBLE?

Christina Mickrenska, Vasil Cvetkov

University of Architecture, Civil Engineering and Geodesy, Hristo Smirnenski Blvd. 1, Sofia, Bulgaria
E-mail: tzvetkov_vasil@abv.bg

Since the end of the 18th century, the basic method for establishing state or continental vertical reference systems has been the precise geometric levelling. Since then, it is supposed that the accuracy of this method is a function of the levelling distance [1, 2, 3]. As a result, the weights applied in the levelling network adjustment are some functions of the levelling line lengths. In addition, based on the Gauss law of error propagation, the mean of both elevation measurements in levelling lines has been preferred as a more plausible value of the measured line elevation.

However, the modern probability theory [4] and popular statistical methods [5] do not support the above levelling assumptions. According to [4], the probability *Cv(n)* that the average of n independent random variables is closer to the distribution expectation than some of the independent variables is a function of the entropy of the standard Normal distribution and the number of variables n. The probability *Cv(n)* can be given by equation (1), where the coefficients a, b, and c depend on the distribution parameters and the number of variables n.

$$Cv(n) = 0.25.\,log_b(2\pi e).\,(n^{-c} - n^{-a}) \tag{1}$$

Based on (1), it can be calculated that in the case of two measurements, i.e., $n = 2$, the probability *Cv(2)* tends to 30% if both measurements are normally distributed. Suppose the situation where both measurements derive from the distribution with the highest entropy, i.e., the Uniform distribution, then *Cv(2)* tends to 33%. Thus, in more than 66% of the cases, the value of one of the two measurements is closer to the true value of the measured quantity in comparison to the mean. Figure 1 illustrates the frequencies of occurrence of the first, the second observation, or their mean, most closely to a known expectation for various distributions [6].

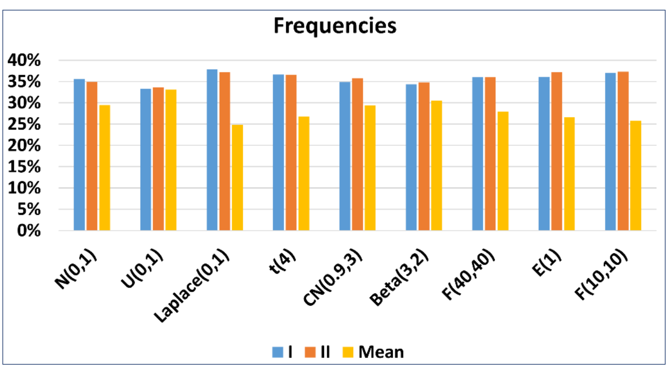

Fig. 1. The frequencies of occurrence of the first, the second observation, or their mean most closely to a known expectation of the applied distributions [6]

The regression analysis of the data obtained in the Third Levelling of Bulgaria /1975–1984/, the Second Levelling of Finland /1935–1955/ [2] and the Third Levelling of Finland /1978–2006/ performed in the study [5] shows that the adjusted coefficient of determination of the absolute discrepancies in levelling lines in respect to the square root of their length, their length L, the sum of the absolute elevations along the lines, and the absolute elevation between line terminal benchmarks |H| are 0.28, 0.34, and 0.26, respectively. In each of the cases, the most significant factor for forming |D|, considering equation (2) is the sum of the absolute elevation values along the lines, which presents the terrain complexity along the levelling lines.

$$|D| = a + b.\sqrt{L} + c.L + d.\sum|h| + e.|H| \quad (2)$$

According to the study [7], there is no significant correlation between the closing errors $|W|$, the loop circumferences L and the square root of L in the above-mentioned levelling networks.

Table 1. Correlation coefficients among the absolute values of the closing errors $|W|$, loop circumferences L and the square root of L in the analysed precise levelling networks [7]

Network	$\rho_{\lvert w \rvert,L}$	$\rho_{\lvert w \rvert,\sqrt{L}}$	$\rho_{L,\sqrt{L}}$
	unitless	unitless	unitless
The Third Levelling of Bulgaria /1975–1984/	0.349	0.348	0.990
The Second Levelling of Finland /1935–1955/	0.104	0.095	0.997
The Third Levelling of Finland /1978–2006/	−0.006	−0.006	0.993

Taking into account all revealed facts, we adjusted the part of the Third Levelling of Finland [3, 6], presented in Figure 2, using a new approach. The basic steps are as follows:

1. Using 3^n independent adjustments, in our case 3^{18} = 387,420,489 adjustments, we selected those values of line elevations among the forwards, the backwards, and their means, which minimised the loop closing errors [6].
2. Using the selected line elevations, we performed an additional 20 independent adjustments to estimate the impact of each line elevation on the network accuracy. In each adjustment, we skipped a different line, and we calculated the sum of the standard errors of the adjusted benchmark geopotential numbers. We skipped a different line in different adjustments and assessed the network accuracy. Based on these results, we formed our weights for each line in the network as a function of the produced accuracy. If a skipped line leads to higher accuracy, we gave it a greater weight in the final adjustment. The weights of each line were calculated as the square of the ratio between the average of the benchmark standard errors in each variant and the average of the benchmark standard errors in all variants.
3. Finally, using the selected elevations in step 1 and their non-parametric and assumption-free weights, obtained as described in step 2, we adjusted the network in Figure 2 as a free levelling network /without a datum point/. Our decision was provoked by the wish to refer the standard errors of the adjusted benchmark geopotential numbers to the network weight centre.

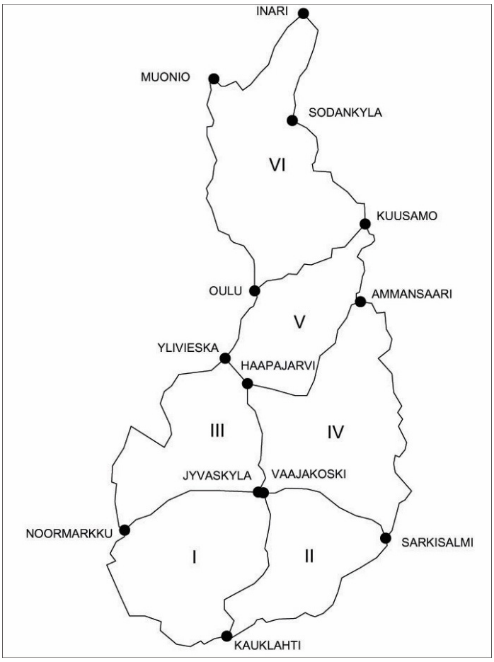

Fig. 2. Scheme of the analysed network, part of the Third Level of Finland network [3, 6]

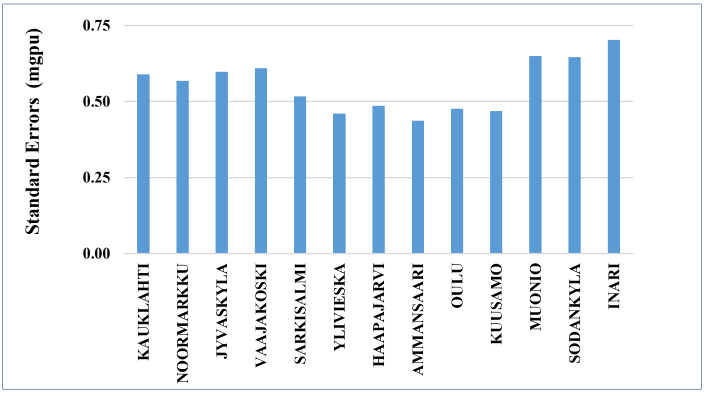

Fig. 3. Standard Errors of the adjusted benchmark geopotential numbers in mgpu

As can be seen from Figure 3, the standard errors of all adjusted benchmark geopotential numbers are below 0.75 mgpu. The adjusted geopotential number of the Ammansaari benchmark has a minimal standard error of 0.44 mgpu. This benchmark is close to the network weight centre. The benchmarks located in the periphery of the network, e.g., Inari, Sodankyla, and Mounio have greater standard errors of the adjusted geopotential numbers, respectively 0.70, 0.65, and 0.65 mgpu. The mean standard error is 0.55 mgpu. The standard deviation of the standard error sample is 0.09 mgpu. Comparison between the standard errors of the adjusted geopotential numbers pictured in Fig. 3 and the standard errors of the adjusted geopotential number of the same benchmarks, but interpolated by Figure 6.3 in the study [3] shows that the uncertainty of a levelling network, adjusted in the manner presented here, can be reduced more than 15–20 times. Taking this fact into account, plus the current progress of the GNSS technologies [1, 8, 9, 10], it is likely that geoid-based vertical reference frames with uncertainty below 10 mgpu can be realised soon.

Acknowledgements

The authors express gratitude to the Centre for Scientific Research and Design at the UACEG for funding and support for the completed research project under contract No BN315/2025 on the topic "Optimisation of levelling networks by studying the applicability of resampling methods."

References

[1] Gerlach, C.; Rummel R. Benefit of classical leveling for geoid-based vertical reference frames. *Journal of Geodesy*. **2024**, *98*(64). https://doi.org/10.1007/s00190-024-01849-y.

[2] Kääriäinen, E. *The Second Levelling of Finland in 1935–1955*. Publications of the Finnish Geodetic Institute No. 61, Helsinki. **1966**.

[3] Saaranen, V.; Lehmuskoski, P.; Takalo M.; Rouhiainen, P. *The Third Precise Levelling of Finland*, FGI Publications No. 161, Kirkkonummi. **2021**. https://helda.helsinki.fi/items/921bf91e-e93d-4ccd-9f83-aac063ee014f.

[4] Cvetkov, V. Averages, entropy and observations. *Deutsche Internationale Zeitschrift Für Zeitgenössische Wissenschaft*. **2024**, *93*, 52–57. https://doi.org/10.5281/zenodo.14289165.

[5] Mickrenska C.; Cvetkov, V. Multiple Regression in Help of the Precise Levelling. *World Summit: Civil Engineering-Architecture-Urban Planning Congress (CAUSummit 2024),* ARPHA Proceedings 7, Pensoft Publishing, Sofia. **2024**, 65–71. https://doi.org/10.3897/ap.7.e0065.

[6] Cvetkov, V. On initial data in adjustments of the geometric levelling networks (on the mean of paired observations). *Journal of Geodetic Science*. **2024**, *14*(1), 20220170. https://doi.org/10.1515/jogs-2022-0170.

[7] Cvetkov, V. A myth concerning the geometric levelling: closing errors and loop circumferences. *Proceedings of 24th International Multidisciplinary Scientific GeoConference SGEM 2024.* **2024**, *24*(2.1), 149–154. https://doi.org/10.5593/sgem2024/2.1/s09.19.

[8] Kurtz, B.; Gómez D.; Bevis, M. Characterization of the precision of PPP solutions as a function of latitude and session length, *Journal of Geodetic Science*. **2024**, *14*(1), 20220176. https://doi.org/10.1515/jogs-2022-0176.

[9] Borowski, L.; Banasik, P.; Maciuk, K. Application of GNSS-levelling for updating the base vertical network, *Journal of Applied Geodesy*. **2025**. https://doi.org/10.1515/jag-2024-0096.

[10] Apollo, M.; Jakubiak, M.; Nistor, S.; Lewinska, P.; Krawczyk, A.; Borowski, Ł.; Specht, M.; Krzykowska-Piotrowska, K.; Marchel, Ł.; Pęska-Siwik, A.; Kardoš, M.; Maciuk, K. Geodata in science – a review of selected scientific fields, *Acta Sci. Pol., Formatio Circumiectus*. **2023**, *22*(2), 17–40. https://doi.org/10.15576/ASP.FC/2023.22.2.02.

GROUND MOVEMENTS IN LATVIA IN 2019–2023 ACCORDING TO THE INTERFEROMETRIC SYNTHETIC-APERTURE RADAR METHOD

Valērijs Ņikuļins

SIA Geo Consultants, Olīvu str. 9, Riga, Latvia
E-mail: seismolat@gmail.com

Knowledge of ground motion is important for selecting a construction site or monitoring the condition of existing critical infrastructure facilities. Modern technologies (GNSS, InSAR) allow obtaining ground motion data with high accuracy, depending on the receivers used (GPS stations), frequency (radar wavelength in the InSAR method), observation conditions and stability of reflecting objects (InSAR points). Ground motion can be caused by tectonic movements, landslides, erosion, ground dissolution and formation of karst voids, frost heaving, thermal fluxion, earthquakes, anthropogenic activities (mining, construction, pumping of groundwater, oil and gas), groundwater, quicksand, deformations due to moisture cycles. Ground motions can be caused by a combination of factors, making it difficult to understand the root cause of ground movement.

The *Ortho* dataset from the *European Ground Motion Service* (EGMS) used for the ground motion analysis. The dataset based on remote sensing from space using the *Sentinel-1* satellite. This dataset includes ascending and descending calibrated products, which averaged over a common 100 m grid. Ground motion analysis based on InSAR (*Interferometric Synthetic-Aperture Radar*) data performed for the territory of Latvia for the period from 2019 to 2023. An active method used, with the emission of its own signal, its reflection from points on the Earth's surface and recording of the scattered energy by a satellite sensor. Horizontal ground motion velocities in the east-west direction and vertical ground motion velocities measured.

The statistical parameters of the InSAR data array estimated. Areas with anomalous values of ground motion identified. The characteristics of the ground motion velocity given for different objects – swamps and peat bogs, quarries, transport highways, settlements.

Statistical results

The range of surface displacement velocity in the study area in the east-west direction (ν_{EW}) varies from –174.7 to +140.5 mm/year, and for vertical movements (ν_{EWR}) it varies from – 134 to + 55 mm/year. The average velocity values are –0.074 mm/year for ν_{EW} and for ν_{EWR} are –0.490 mm/year. The standard deviations are 2.371 mm/year for ν_{EW} and 2.489 mm/year for ν_{EWR}, respectively. Negative skewness of the distribution of movement velocities ν_{EW} (–0.226) and ν_{EWP} (–1.538) is noticeable. The normal distribution function does not perfectly reflect the experimental distribution. A better approximation to the experimental distribution provided by the probability density function based on the *t Location-Scale* and *Non-Parametric* distributions.

Peatlands

The results of ground movement in the area of some peatlands were unexpected. The ground movement speeds in them often have anomalous vertical and horizontal values. The cause of this effect may be the technology of peat collection and storage. Various methods of peat collection used, including cutting peat briquettes. It is possible that individual pieces of peat have good properties for reflecting electromagnetic radiation (EMR). In some cases, for example, in the area of Lake *Lubāna*, there are several peatlands with opposite directions of movement (Fig. 1). The cause of peat movement may be associated with changes in the level of groundwater and greenhouse gas emissions from peat soils [1], i.e. with the so-called "breathing" of the bogs.

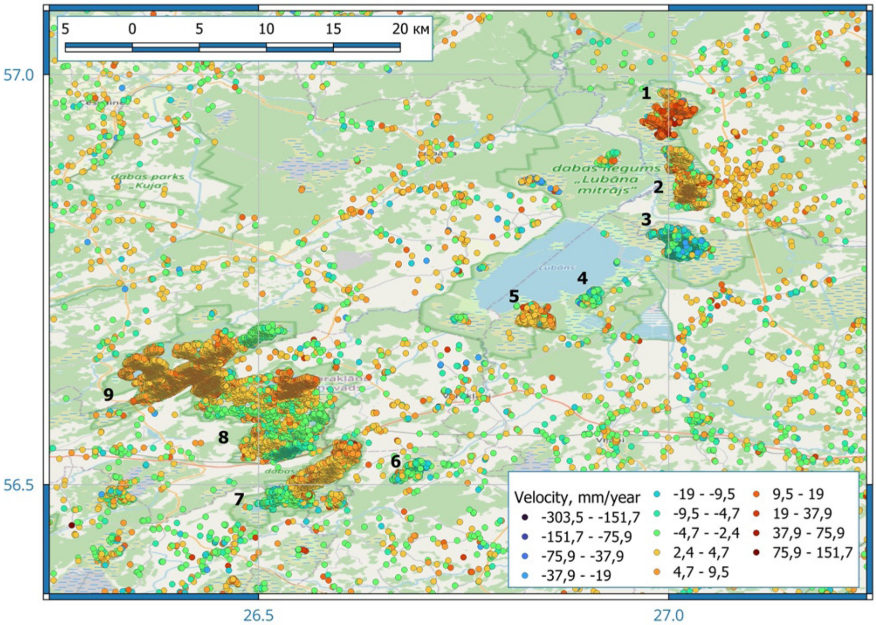

Fig. Horizontal ground movement velocities in the east-west direction in the area of Lake *Lubāna*

Quarries

Some industrial quarries have also proven to be good objects for reflecting EMI. The most probable reason for this is the removal of the upper, loose layer of Quaternary deposits, under which denser rock deposits are located, most often Devonian. Deposits of dolomite, limestone and gypsum represent these rocks. A typical example is the *Kūmas* quarry, where limestone mined, or the *Salaspils* quarry, where gypsum mined.

Transport highways

Transport highways are good objects of EMR. First, these are railways and, to a lesser extent, highways. For example, sections of the railway in the *Bolderaja* area, in the direction to the north and to the northeast, with a length of 2.9 km and 1.8 km, respectively, are sinking at velocities from 4.7 to 21.3 mm/year.

Populated areas

The largest number of good objects (InSAR points) of EMR are located in populated areas. Such objects are roofs of buildings, roads, concrete structures and other objects characterized by good reflective properties for EMR. The largest subsidence areas have a complex, mosaic shape and randomly distributed in Riga and its environs. The velocities of ground subsidence within these areas vary from – 2.5 to – 27.0 mm/year. The most intense subsidence areas are located along the railway on the right bank, as well as in the southern part of *Kundziņsala*. The rest of the territory of Riga is mainly characterized by uplift with rates from 0 to 5 mm/year.

Comparison of the results of the EGMS (2019–2023) and PanGeo (1992–2000) projects

The *PanGeo* project was carried out within the framework of the 7th Framework Program of the European Union from 2011 to 2013. The objective of the project was to assess geological hazards in support of the *Copernicus* program (formerly GMES – *Global Monitoring for Environment and Security*). These assessments are based on the collection of environmental data via *the European Space Agency* (ESA) satellites, as well as other data from the *European Environment Agency* (EEA). Ground stability layers created within the *PanGeo* project. This product is based on the joint processing of InSAR data, geological information and information on geological, tectonic hazard factors from European geological services. The vertical movement velocities used to identify geological hazard polygons.

Geological assessments based on the integration of the above data performed for Riga and Liepaja for the period from 1992 to 2000 for Latvia. Reflections for 64,116 InSAR points obtained in the territory of Riga. 57 geological hazard polygons were identified [2]. The main features for identifying the polygons were the concentration of InSAR points. According to the *PanGeo* project data, the central part of Riga, bounded by *Sarkandaugava* to the north and *Krišjāna Valdemāra* and *Duntes* streets to the south and east, has a predominant subsidence trend. In the southeast from this area, in the center of Riga, InSAR points with positive velocity predominate.

The EGMS project results for the *Ortho* dataset of this area of Riga and the time interval from 2019 to 2023 do not show this uplift. In addition, the *Ortho* dataset results do not reflect the extreme values of vertical velocities for other polygons identified in the *PanGeo* project (1992–2000). The *PanGeo* project results characterize tectonic movements better than EGMS project with Orto dataset.

References

[1] Hrysiewicz, A.; Williamson, J.; Evans, C. D.; Jovani-Sancjo, A. J.; Callaghan, N.; Lyons, J.; White, J.; Kowalska, J.; Menichino, N.; Holohan, E. P. Estimation and validation of InSAR-derived surface displacements at temperate raised peatlands. *Remote Sensing of Environment.* **2024**, *311*, 1–24. https://doi.org/10.1016/j.rse.2024.114232.

[2] Nikulin, V. Geological hazard zones for Liepaja and Riga based on the results of remote sensing by the Persistent Scatterer Interferometry method. (In Russian). *Sabiedrība un kultūra.* **2014**, *XVI*, 432–439.

ON THE RELATIONSHIP BETWEEN GROUND MOTION BASED ON INSAR DATA, THE 2021 EARTHQUAKES IN GREECE AND THE COSSEISMIC PHENOMENON

Valērijs Ņikuļins[1], Dmytro Malytskyy[2]

[1] *SIA Geo Consultants, Olīvu str. 9, Riga, Latvia*

[2] *Carpathian Branch of Subbotin Institute of Geophysics, National Academy of Sciences of Ukraine, 3-b Naukova str., 79060 Lviv, Ukraine*

E-mail: seismolat@gmail.com

The aim of the study was to find a connection between slow movements and earthquakes in a seismically active region. The connection between fast (earthquakes) and slow (tectonic creep) motions is important in terms of searching for earthquake precursors. The study of such a connection based on an integrated approach that combines high-density geodetic observations (GNSS or SAR) and seismological information [1].

The initial information for assessing slow motions was data from the Copernicus Earth observation service, part of the *European Union's Space Programe*. The Ortho 2019–2023 vector product for ascending and descending orbits of the *European Ground Motion Service* used. Ground motion parameters (velocities and displacements) in the vertical direction and in the horizontal direction (east west) for different azimuths from the earthquake epicenter obtained using the InSAR (*Interferometric Synthetic Aperture Radar*) method.

The research object is located in Greece. The territory of Greece is a seismically active region where strong earthquakes occur. The main shock with a magnitude of 6.3 (20210303–101609) and subsequent aftershocks occurred in northern Thessaly (central Greece). The seismotectonic setting in the research area characterized by the predominance of extension in the north-south direction. In the central part of the research area, the faults have a normal faulting mechanism and form a graben-like structure [2].

Among 19 aftershocks with magnitudes greater than 3.7, the first aftershock (20210304–183820) with a magnitude of 6.0 occurred one day after the main shock. The main shock and the first aftershock were the strongest earthquakes in this area since 1941. The mechanism of the analyzed earthquakes is predominantly of a normal faulting. However, among 19 aftershocks there are earthquake focal mechanisms with a strike-slip component: *Normal Right-Lateral Oblique*, *Normal Left-Lateral Oblique*.

Because of the main shock impact and possibly also under the influence of the first aftershock, a depression zone (Fig.) of about 123 km^2 (16 × 10 km) in size was formed as result of coseismic and/or early post-seismic subsidence phenomenon. The zone extends in the northwest-southeast direction and surrounded by the *Larisa* and *Tyrnavos* faults in the northeast and the *Pineias* fault in the south – southeast. The planes of the first two faults dip to the northeast, and the third fault dips to the southeast [2]. In the central part of the depression zone, the maximum vertical subsidence velocity reached 128 mm/year, and the sharp displacement after the main shock reached 131 mm (as of 20210303). Subsequent subsidence occurred due to aftershock activity and subsequent aseismic creep, and reached

425 mm in October 2023 (2023–1007). The maximum horizontal velocity in the east-west direction reached 56 mm/year. The amplitude of a sharp change in the direction of displacement from west to east occurred on March 3, 2021 and reached 285 mm.

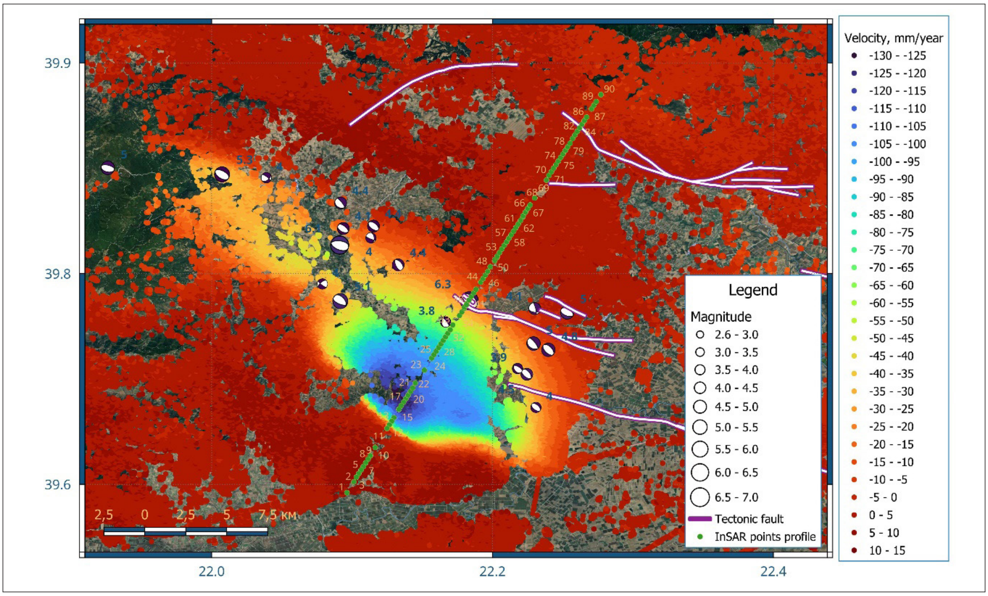

Fig. Seismotectonic setting and vertical motion velocities after the earthquake of 03.03.2021 (10:16:09 GMT) with magnitude of 6.3 in Greece

The gradient zone of ground displacement velocities well revealed based on vertical velocities and much weaker based on horizontal velocities. The gradient zone can be an indicator of a fault zone oriented from northwest to southeast with an azimuth of about 140°.

The orientation of maximum horizontal stresses is important for understanding the dynamics of the earth's crust. The orientation of the *P*-axes of the earthquake focal mechanisms allowed us to estimate of indirectly the directions of horizontal stresses. The parameters of the *P*-axes (azimuth and angle of incidence) obtained based on the solution of the focal mechanisms of the main shock and the 19 subsequent aftershocks. The orientation of horizontal stresses supplemented by an estimate of their conditional value. This parameter gives an idea of the stress-strain state of the geological environment and shows the influence (contribution) of earthquakes on the process of depression zone formation.

The *Coulomb* stress variation on adjacent receiving faults estimated. The main shock stress release at its source contributed to the occurrence of increased stress at both ends of the *Tyrnavos* fault. The proposed *Coulomb* stress variation model showed an increase in stress at the northwestern end of the *Tyrnavos* fault, where the first strongest foreshock with a magnitude of 6.0 occurred.

Conclusions

1. The main shock 2021/03/03 (10:16:09 GMT) led to the formation of a depression zone, in which the subsidence process continued until October 2023 probably due to foreshock seismic activity and tectonic creep.

2. The depression zone identified using the InSAR synthetic aperture interferometric method based on vertical velocity of ground motion data.
3. The band with a high gradient of change in the velocity of vertical ground motions according to InSAR data in the southwestern part of the depression zone may be an indicator of an active tectonic fault extending for a distance of about 10 km from northwest to southeast at an azimuth of approximately 140°.

References

[1] Crespi, M.; Kossobokov, V.; Peresan, A.; Panza G.F . Chapter 5 – The integration between seismology and geodesy for intermediate-term narrow-range earthquake prediction according to NDSHA. *Earthquakes and Sustainable Infrastructure*. **2022**, 97–112.

[2] Papadimitriou, E.; Karakostas, V.; Papazachos, C.; Foumelis, M.; Kiratzi, A.; Pikridas, C.; Bonatis, P.; Kostoglou, A.; Kourouklas, C.; Scordilis, E.; Bitharis, S.; Paradisopoulou, P.; Panou, A.; Galanis, O.; Karagianni, E.; Vamvakaris, D.; Karagianni, I.; Kkallas, C.; Chatzis, N.; Chatzipetros, A.; Fotiou, A.; Ventouzi, C.; Grendas, I.; Kementzetzidou, D.; Karakaisis, G.; Hatzidimitriou, P. The seismogenic structure of March 2021 Tyrnavos (central Greece) doublet (Mw 6.3 and Mw 6.0), constrained by afterschock locations and geodetic data. *Geophysic Journal International*. **2023**, *235*, 644–689. https://doi.org/10.1093/gji/ggad253.

THE FOCAL MECHANISM SOLUTION OF MARSQUAKES BY INVERSION OF P- AND S- WAVES

Dmytro Malytskyy[1, 2], Andriy Gnyp[1], Oleksandra Astashkina[1], Markiyan Dobushovskyy[1], Ruslan Pak[1], Valērijs Ņikuļins[3]

[1] *Carpathian Branch of Subbotin Institute of Geophysics, National Academy of Sciences of Ukraine, 3-b Naukova str., 79060 Lviv, Ukraine*

[2] *Institute of Rock Structure and Mechanics, Academy of Sciences of the Czech Republic, Prague, Czech Republic*

[3] *SIA Geo Consultants Olīvu str. 9, Riga, Latvia*

E-mail: dmalytskyy@gmail.com

Seismic data recorded by the SEIS experiment [1] onboard the InSight mission [2] have shown that Mars is seismically active with more than 1300 events detected and catalogued by the InSight Marsquake Service (MQS) [3]. The seismometer on board NASA's Mars InSight mission has discovered a seismically active planet. We focus on a few events that were recorded by the very wide-range sensors and the associated ELYSE channel, located 37.2° from InSight. We use a method based on the point source approach for elastic horizontal-layered media to obtain source parameters for seismic events on Mars. In this case, the seismic moment tensor inversion of high-frequency seismogram data is calculated using a matrix method for direct waves. The process involves generating offset records using a frequency-wavenumber integration technique. A method for inverting the moment tensor of direct P- and S-waves, which are less sensitive to path effects than reflected and transformed waves, is presented, which significantly improves the accuracy and reliability of the method [4, 5].

We propose to invert only the direct waves instead of the full field. An advantage of inverting only the direct *P*- and *S*- waves is that, compared to reflected and converted waves, they are less sensitive to the structural model used in the inversion. For example, waveforms of converted and reflected waves depend strongly on velocity contrasts below the source and receiver, and thus imprecise knowledge of subsurface structure will lead to inaccurate modelling. Waveforms of direct phases are less sensitive to subsurface layering, scattering and may carry a less distorted imprint of the source. The advantage of choosing a matrix method for calculating synthetic seismograms is its ability to analytically isolate direct waves from the full wave field. In the earlier version of our method, as well as in most other MT inversions, waveforms at several seismic stations are simultaneously inverted [4, 5]. Although much more information on the source should be contained in the waveforms from several stations, we show nevertheless in our study that all the components of seismic moment tensor contribute to the waveforms at only one station and, at least theoretically, can be retrieved from them, a possibility explored in a current version of the inversion. We use a point-source approximation, assuming the location and origin time proposed by [6]. We first present the focal mechanism of the S0235b event on Mars (July 26, 2019), located 25° from the epicenter [6]. We compare two methods: in the first we propose to invert only direct waves [7], and in the second we consider direct inversion for the full moment tensor [8]. We tried three different source depths: 17 km, 32 km and 56 km. The TAYAK velocity model was used [7, 8]. The durations of direct *P*- and *S*- waves at the station are estimated visually from the records and delays of the reflection-conversion phases at the respective epicentral distance and source depth are considered. The focal mechanisms for the source depth of 32 km shown in Figure 2 look very similar to each other.

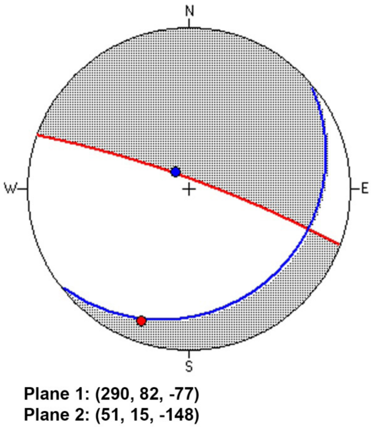

(a)

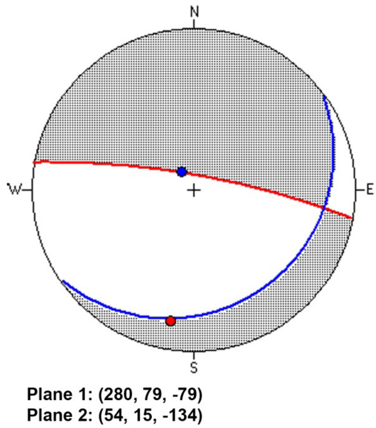

(b)

Fig. 1. Focal mechanisms of the S0235b event obtained by inversion of only direct waves [7] (a) and by direct inversion for the full moment tensor [8] (b) for a source depth of 32 km

We also present the inversion results for the S1222a event on Mars (2022-05-04, *P*-arrival 23 : 27 : 45, 3 : 54 LMST, M_w 4.7, back azimuth 109°) which is located on Aeolis Southeast at 37.2° distance from InSight [6]. The component of moment tensor resulting from the inversion of the direct *P*- and *S*- waves forms at only the station ELYSE. The corresponding focal mechanism are shown in Figure 2.

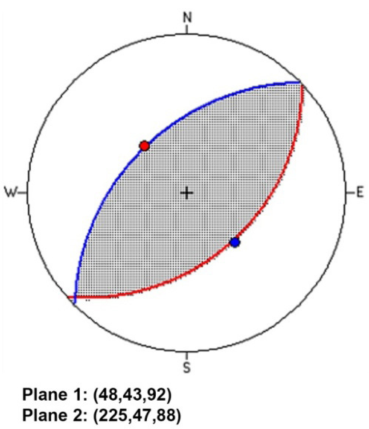

Fig. 2. Version of the focal mechanism solution for the S1222a event on Mars (2022-05-04, M_w 4.7, back azimuth 109°) [7]

Acknowledgments

The work presented in this paper was partially supported by the Institutional Research Plan RVO67985891 of the Institute of Rock Structure and Mechanics of the Czech Academy of Sciences and the program CAS Researchers at Risk Fellowship 1598/2024 OMS.

References

[1] Lognonné, P.; Banerdt, W.; Pike, W. T.; Giardini, D.; Christensen, U.; Garcia, R. F., et al. Constraints on the shallow elastic and anelastic structure of Mars from InSight seismic data. *Nature Geoscience*. **2020**, *13(3)*, 213–220. https//doi.org/10.1038/s41561-020-0536-y.

[2] Banerdt, W. B.; Smrekar, S.; Banfield, D.; Giardini, D.; Golombek, M. P.; Johnson, C., et al. Initial results from the insight mission on Mars. *Nature Geoscience*. **2020**, *13(3)*, 183–189. https://doi.org/10.1038/s4156-020-0544-y.

[3] Giardini, D.; Lognonné, P.; Banerdt, W. B.; Pike, W. T.; Christensen, U.; Ceylan, S., et al. The seismicity of Mars. *Nature Geoscience*. **2020**, *13,* 205–212. https:/doi.org/10.1038/s41561-020-0539-8.

[4] Malytskyy, D. Mathematical modeling in the problems of seismology. *Naukova Dumka*. **2016**, Kyiv, 277 (in Ukrainian).

[5] Malytskyy, D. & D'Amico, S. Moment tensor solutions through waveforms inversion. *Mistral Service S.a.S.*, *Earth and Enviromental Sciences.* **2015**. ISBN 978-88-98161-13-3.

[6] Kawamura, T.; Clinton, J. F.; Zenhausern, G.; Ceylan, S.; Horleston, A. C.; Dahmen, N. L. S1222a- the largest Marsquake detected by InSight. *Geophysical Research Letters*. **2022**. https://doi: 10.1029/2022GL101543.

[7] Malytskyy, D.; Křížová, D.; Lognonné, P.; Kawamura, T.; Perrin, C.; Plasman, M.; Xu, Z.; Maguire, R. High- and Low-Frequency Waveform Analysis the Marsquake of Sol 1222: Focal Mechanism, Centroid Moment Tensor Inversion and Source Time Function. *Earth and Space Science*. **2024**, *11*, e2023EA003272, https://doi.org/10.1029/2023EA003272.

[8] Brinkman, N.; Stähler, S. C.; Giardini, D.; Schmelzbach, C.; Khan, A.; Jacob, A., et al. First focal mechanisms of marsquakes. *Journal of Geophysical Research: Planets*. **2021**, *126(4)*, e2020JE006546. https://doi.org/10.1029/2020JE006546.

FIRST RESULTS OF ATMOSPHERIC ANOMALOUS REFRACTION RESEARCH USING THE DIGITAL ZENITH CAMERA VESTA

Inese Varna, Ansis Zarins, Gunars Silabriedis, Ingus Mitrofanovs, Augusts Rubans, Druvis Kleins, Ivars Bergmanis

University of Latvia, Institute of Geodesy and Geoinformatics, Jelgavas str. 3, Riga, Latvia
E-mail: inese.varna@lu.lv

Digital zenith camera (DZC) VESTA (VErtical by STArs) is a complex astrogeodetic instrument for measuring deflections of vertical (DoV) – angle between ellipsoid normal and plumb line. DoVs characterize Earth's gravity field, representing inclination of geoid surface to reference-ellipsoid surface. DZC VESTA main components are vertically oriented 8-inch telescope, an electronic high resolution two-axis tiltmeter, a GNSS receiver, a CCD camera, linear actuators and an embedded computer. Measurements are performed at night, using images of the observed stars and star catalogue data as high accuracy reference.

Even during the initial tests of this instrument, temporal variations of DoV were noticed; these variations have been present in all subsequent DoV measurements [1]. One possible source of these variations is assumed to be atmospheric anomalous refraction (AR), a phenomenon known to affect ground-based astrometric observations [2, 3, 4, 5]. AR causes irregular angular displacements of observed stars. It can result in variations with amplitudes of up to 0.2–0.5 arcseconds and periods ranging from tens of minutes to several hours; a shorter-period manifestation of AR is the common twinkling of stars. The literature also mentions the possibility of longer—seasonal—or even persistent effects. Because a typical VESTA measurement session lasts around 40–60 minutes, AR can significantly degrade DoV measurement accuracy.

In 2025, a new project "Investigation of anomalous refraction effect by using automated digital zenith camera VESTA" was started at the University of Latvia. This project aims to deepen the understanding of AR behaviour using DZC VESTA and to search for solutions to mitigate its impact on astrometric observations.

Long overnight measurement campaigns will be conducted in various environments: open flat fields, hilly areas, and coastal locations, during all seasons and under different weather conditions. Different environmental settings may reveal distinct AR characteristics; for example, on hill slopes, the inclination of atmospheric layers may influence AR behaviour. It is also planned to carry out overnight campaigns using two adjacent DZCs to differentiate between instrument-induced variations and actual changes in the measured quantity, and to determine the spatial properties of AR effects.

To better understand the vertical distribution of AR, meteorological data recording equipment will be used. A network of meteorological sensors recording temperature, humidity, and pressure will be set up around the DZC observation site during measurements.

Since the beginning of the project, three observation sites have been selected: Lode (hilly area), Tīnūži (flat, open field), Tūja (coastal area). Regular overnight observations have started in Lode, primarily for testing the DZC and meteorological sensor network setup. The first results reveal high variability between different nights of observation. This variability may be typical of early spring; in previous campaigns, this period was usually avoided due to unsuitable weather conditions and a low number of stars in the zenith. Results from the Lode observations are shown in Figure.

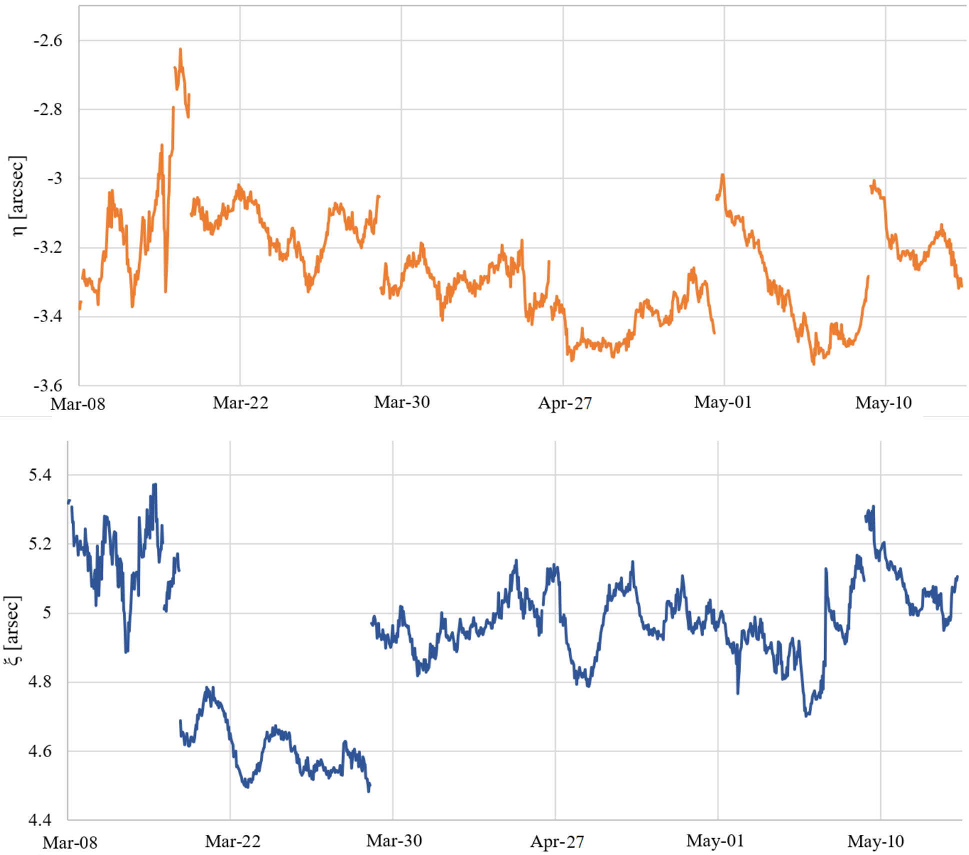

Fig. VESTA 30-position (~ 40 min) time window solutions of both deflection of the vertical components at Lode – multiple overnight observations during March–May 2025

References

[1] Zariņš, A.; Rubans, A.; Silabriedis, G. Performance analysis of Latvian zenith camera. *Geodesy and Cartography*. **2018**, *44*(1), https://doi.org/10.3846/gac.2018.876.

[2] Hirt, C. Monitoring and Analysis of Anomalous Refraction Using a Digital Zenith Zamera System. *Astron. Astrophys*. **2006**, *459*(1), 283–290. https://doi.org/10.1051/0004-6361:20065485.

[3] Hirt, C.; Seeber, G. Accuracy Analysis of Vertical Deflection Data Observed with the Hannover Digital Zenith Camera System TZK2-D. *J. Geod*. **2008**, *82*(6), 347–356. https://doi.org/10.1007/s00190-007-0184-7.

[4] Hirt, C.; Bürki, B.; Somieski, A.; Seeber, G. Modern Determination of Vertical Deflections Using Digital Zenith Cameras. *J. Surv. Eng*. **2010**, *136*(1), 1–12. https://doi.org/10.1061/(ASCE)SU.1943-5428.0000009.

[5] Guillaume, S. Determination of a Precise Gravity Field for the CLIC Feasibility Studies, PhD Thesis. Eidgenössische. **2015**.

FOSTERING RESILIENCE TO CLIMATE CHANGE – CARMINE PROJECT

Iuliana Maria Pârvu, Iuliana Adriana Cuibac, Adrian Grigore Pârvu, Nicoleta Pârvulescu

National Center for Cartography, Bd Expoziției 1A, Bucharest, Romania
E-mail: iuliana.parvu@cartografie.ro

The CARMINE project (Climate-Resilient Development Pathways in Metropolitan Regions of Europe) is funded by Horizon Europe and seeks to enhance the resilience of European metropolitan areas to climate change. By co-developing knowledge-based tools, strategies, and action plans, CARMINE aims to support adaptation and mitigation efforts aligned with the EU's Mission on Climate Change Adaptation for 2030 [1]. The project adopts an interdisciplinary, co-creation approach, fostering collaboration between scientific research, local authorities, civil society, and other key stakeholders to develop actionable knowledge, decision-support tools, and integrated adaptation plans. The main objectives of the project are to: provide knowledge-based Climate Resilient Development Pathways in Metropolitan Regions of Europe, deliver impact-based decision support services and guidance services for increased resilience and adaptive capacity, including early warning systems and disaster risk management and ensure science-based R&I solutions for multi-level climate governance that support local adaptation assessments and plans.

CARMINE will be implemented in eight metropolitan regions across Europe: Prague (CZ), Leipzig (DE), Funen-Odense (DK), Athens (EL), Barcelona (ES), Bologna (IT), Brașov (RO), and Birmingham (UK). This geographical diversity ensures that the findings are transferable across different climate zones, socio-economic contexts, and urban governance systems. The National Center for Cartography (CNC) contributes to various work packages, focusing on climate risk assessments, socio-economic vulnerability evaluations, and the development of a 3D building model to improve resilience in urban governance. The Romanian case study is conducted in Brașov Metropolitan Area, where flood risk assessment is carried out using high-resolution geospatial and meteorological data [2].

The tests derived were performed using four flood scenarios. In this sense, we increased the river water levels with 0.5 m, 1 m, 2 m, and 3 m. The simulations relies on a 2-meter resolution Digital Terrain Model (DTM) and the topographic vector data from the national TopRO5 database. The outputs of this analysis include:

- vector maps of flooded areas under each scenario;
- statistical data on affected areas, categorized by land use class (e.g., residential, industrial, agricultural);
- detailed flood maps for urban and rural zones, providing key inputs for emergency calling and land-use planning.

The analysis done for the area affected by floods displayed by land cover includes classes like: forest, protected areas, agricultural land, artificial surfaces, and semi-natural areas. The study demonstrates that agricultural areas, that occupy most of the rural area, are the most affected by floods when the water level rises by 3 meters. These statistics underscore the critical importance of flood management and land-use planning in the Brașov region, especially concerning agricultural productivity and conservation of natural and protected areas.

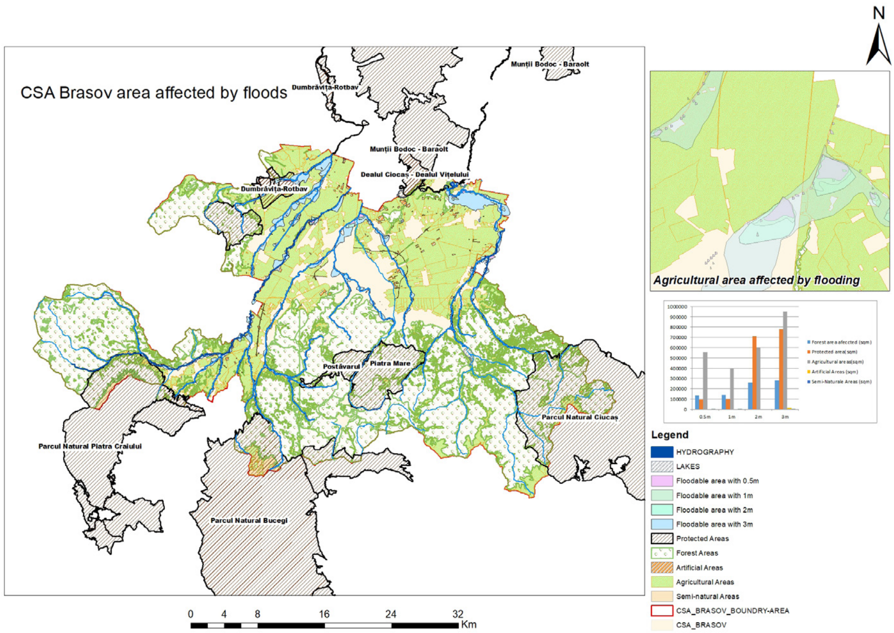

Fig.1. Land use flood area in four scenarios

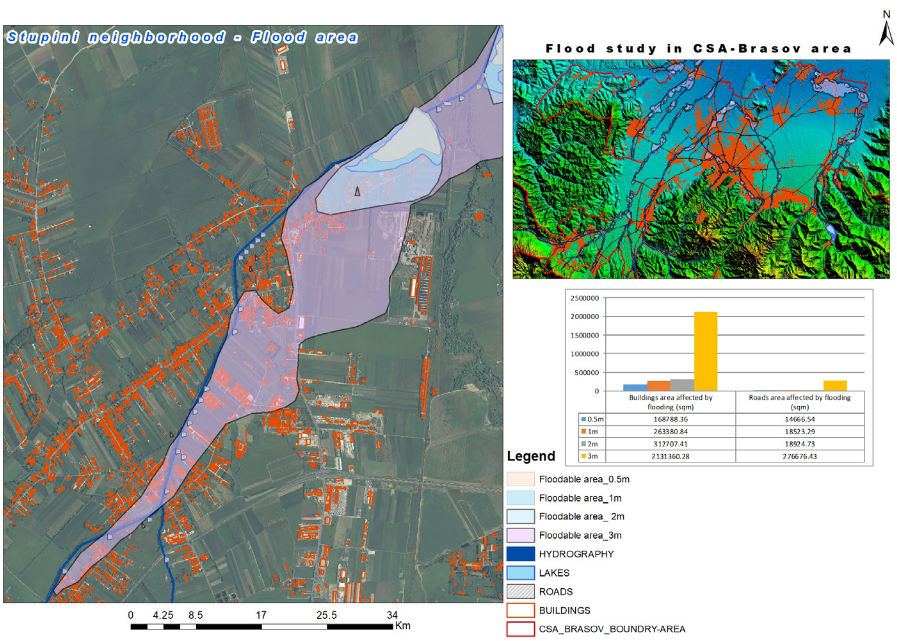

Fig. 2. Flood areas in an urban area

From Fig. 2., we can conclude that the area affected grows exponentially if the water level increases. For the 3 meters increase of the water level the area covered by affected buildings reaches 2 kmp.

To enhance spatial accuracy, 3D building models for the Brașov test area were derived using digitized building footprints extracted from an orthophoto of 8 cm spatial resolution [3].

Fig. 3. Test area for the 3D building models

These models will enable advanced simulation of water propagation and damage estimation at building level. The integration of 3D building models with meteorological data (e.g., rainfall, humidity, and runoff) supports the simulation of urban flood scenarios under different climate conditions. These simulations allow: identification of high-risk areas based on terrain and the storm water pathways, generation of flood risk maps that highlight potential collecting water zones and water flow routes and evaluation of the effectiveness of current drainage infrastructure and green adaptation strategies [4].

By comparing DTM data with forecasted rainfall events, local authorities can proactively plan interventions to reduce the exposure of critical infrastructure and vulnerable populations. These tools also support emergency planning by indicating which buildings and zones are at risk during specific rainfall intensities.

Following this study, authorities and project partners will identify and incorporate nature-based solutions – such as green infrastructure, permeable surfaces, urban wetlands and restoration of natural watercourses – in the decisions plans that will improve the effectiveness of traditional approaches. These solutions not only mitigate flood risks, but also provide corresponding benefits for biodiversity, air quality and urban places.

References

[1] CARMINE Consortium. GRANT AGREEMENT-101137851-CARMINE. **2023**.

[2] Blöschl, G.; Gaál, L.; Hall, J., Kiss, A.; Komma, J., Nester, T.; Parajka, J.; Perdigão, R. A. P.; Plavcová, L.; Rogger, M.; Salinas, J. L.; Viglione, A. Increasing river floods: fiction or reality? *WIREs Water*. **2015**, *2*(4), 271–424.

[3] Pârvu, I. M.; Cuibac Picu, I. A.; Pârvu, A.; Cristache. M. Modelling photogrammetric dataset in order to enhance urban planning. *Proceedings of the International Symposium "Forest and Sustainable Development"*. **2025**. in publication.

[4] Nkwunonwo, U. C.;Whitworth, M.; Baily, B. A review of the current status of flood modelling for urban flood risk management in the developing countries. *Elsevier B.V.,* **2020**.

MACHINE LEARNING–ENHANCED GEOID ESTIMATION FROM TERRESTRIAL AND SATELLITE DATA

John Akutcha, Ahmed Abdalla

Department of Civil and Environmental Engineering, Louisiana State University, LA 70803, Baton Rouge, USA
E-mail: jakutc1@lsu.edu

Accurate orthometric height is a fundamental requirement in geodesy, as well as in a wide range of geophysical and engineering applications. Orthometric height is defined relative to mean sea level (MSL), which is closely approximated by the geoid, a complex, equipotential surface representing the Earth's gravity field. Traditionally, orthometric heights are determined using precise leveling, which yields height differences with high relative accuracy. However, despite its precision, this technique is labor-intensive, time-consuming, and often impractical for extensive or inaccessible regions. In contrast, modern Global Positioning System (GPS) technology enables rapid and accurate position determination, but the heights it provides are relative to a reference ellipsoid, a simplified mathematical model of the Earth's shape [1]. For practical and scientific purposes, these ellipsoidal heights must be transformed into orthometric heights to relate measurements to the physical surface of the Earth and to ensure consistency with existing geodetic and engineering frameworks.

The geoidal height, or undulation, indicates the vertical separation between the geoid and the reference ellipsoid. This measure is essential for modern height systems as it facilitates the conversion of GPS-derived ellipsoidal heights into orthometric heights. Orthometric heights are referred to as mean sea level and are commonly used in geodetic, engineering, and mapping applications. The geoid represents the Earth's gravity field and approximates mean sea level, while the ellipsoid is a smooth, mathematically defined reference surface utilized by satellite positioning systems. Determining geoidal height is crucial for integrating GPS data with traditional leveling networks. This can be accomplished using geometric methods that leverage co-located GPS and leveling data. Alternatively, gravimetric methods rely on gravity observations and physical modeling or applying Global Geopotential Models (GGMs). GGMs combine satellite and terrestrial gravity data to produce global estimates of the geoid at various resolutions. These approaches facilitate consistent height referencing at local, regional, and global scales.

GGMs represent the Earth's gravitational potential through spherical harmonic expansions, enabling the computation of geoid undulations with global coverage. These models are constructed using a combination of satellite-based gravity missions, such as the Gravity Recovery and Climate Experiment (GRACE) and the Gravity field and steady-state Ocean Circulation Explorer (GOCE), along with terrestrial and marine gravimetry, airborne gravity surveys, and satellite altimetry. GGM accuracy varies with spectral content due to factors such as spatial resolution and noise measurement. This study analyzes five recent ultra-high-degree GGMs, namely, XGM2019e, GECO, EGM2008, SGG-UGM-2, and EIGEN-6C4, obtained from the International Centre for Global Earth Models (ICGEM) [3], complete to degree and order 2190, focusing on geoid undulations from degree 5 and upwards. Machine learning techniques are used to correct discrepancies between GGM-derived undulations and control point observations, improving geoid estimation accuracy [4].

This study assesses the accuracy of GGMs by comparing gravimetric geoid undulations with geometric geoid undulations computed from GPS and leveling data at 5,379 benchmarks across the United States. The GPS/Levelling dataset used for this research is obtained from the National Geodetic Survey (NGS) website [2]. The gravimetric undulations are derived through spherical harmonic synthesis of the GGM, incorporating topographic corrections, while the geometric undulations represent observed differences between ellipsoidal and orthometric heights. Residuals between the two are analyzed as a function of spherical harmonic degree to quantify model errors. Statistical measures such as RMSE, mean bias, and standard deviation are used to evaluate each GGM's fidelity. The analysis identifies the optimal truncation degree that minimizes residuals and establishes a foundation for hybrid geoid modeling using residual interpolation or machine learning.

The results show that the lowest Root Mean Square Error (RMSE) values for the GGMs were consistently noted at a maximum degree and order (d/o) of 2140. The best RMSE was 62.75 cm from XGM2019e_2159, while the worst was 63.31 cm from EGM2008, resulting in a minimal difference of 0.56 cm across models. The other models, SGG-UGM-2 (62.93 cm), GECO (63.07 cm), and EIGEN-6C4 (63.09 cm), showed similar performance, indicating convergence at fine spectral scales. The RMSE differences between d/o 2140 and 2190 were negligible, between –0.27 mm and –1.01 mm, suggesting limited gains in predictive accuracy beyond d/o 2140. In contrast, RMSE reductions between d/o 720 and 2140 were substantial, ranging from –20.6 mm to –25.7 mm. Overall, these findings indicate that increasing GGM resolution beyond d/o 2100 offers only minor improvements relative to computational costs.

Figure 1 (Left) shows the RMSE trend of the GGM-derived geoid undulations from d/o 5 to 2190, and Figure 1 (Right) shows the log of the RMSE values from d/0 360 to 2190.

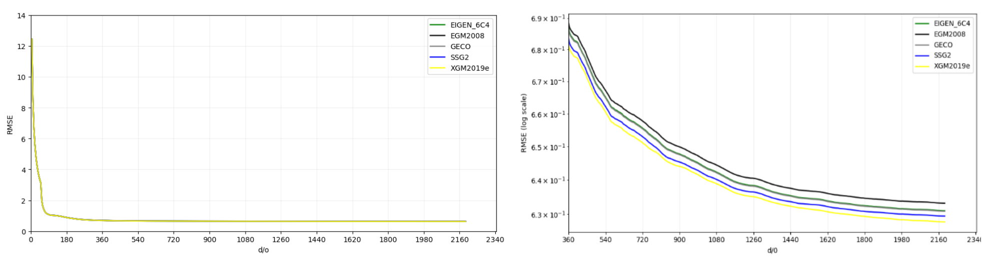

Fig. 1. RMSE comparison of Residuals Between GGMs and GPS/Levelling geoid
Left: RMSE (d/o 5 to 2190). Right: Log RMSE (d/o 360 to 2190).

The results show that while high-degree GGMs generally offer good accuracy, their differences diminish at higher degrees, indicating a convergence in representing the Earth's gravity field. However, improvements are needed to lower residual errors, especially in root mean square error (RMSE). Recent machine learning advancements promise enhancements in modeling geoid undulations by capturing complex relationships not addressed by traditional methods. Three ML algorithms, Support Vector Regression (SVR), Random Forest (RF), and Multilayer Perceptron (MLP), were tested at 5-degree intervals up to degree 2190, with 80% of the data for training and 20% for testing. These models significantly improved predictive accuracy, with MLP consistently outperforming SVR and RF, achieving the lowest RMSE and highlighting the potential of deep learning in refining geoid models.

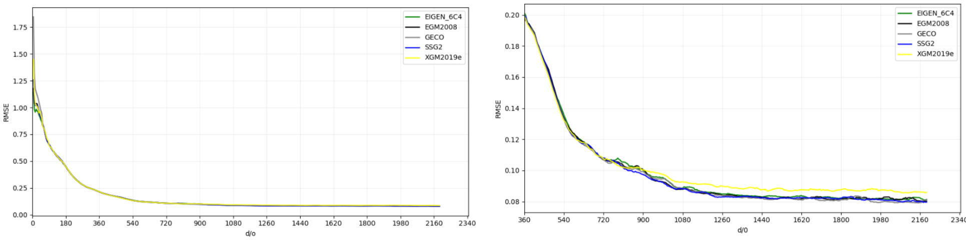

Fig. 2. RMSE comparison of Residuals after MLP
Left: RMSE (d/o 5 to 2190). Right: RMSE (d/o 360 to 2190)

Figure 3 shows the RMSE trends before and after applying the MLP. It can be seen that the application of MLP significantly reduced RMSE values across all GGMs for all d/o.

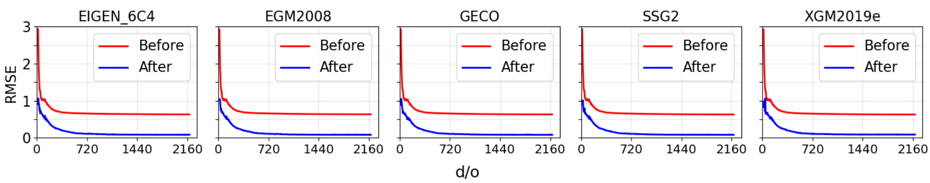

Fig. 3. RMSE comparison of residuals before and after applying MLP

Figure 4 also shows the histogram of the residuals before and after the MLP at the d/o that achieved the lowest RMSE after the MLP was applied. It can be seen that MLP reduced the residual spread from approximately ± 1.6 m to less than ± 0.5 m, significantly improving the accuracy of GGM-derived geoid undulations.

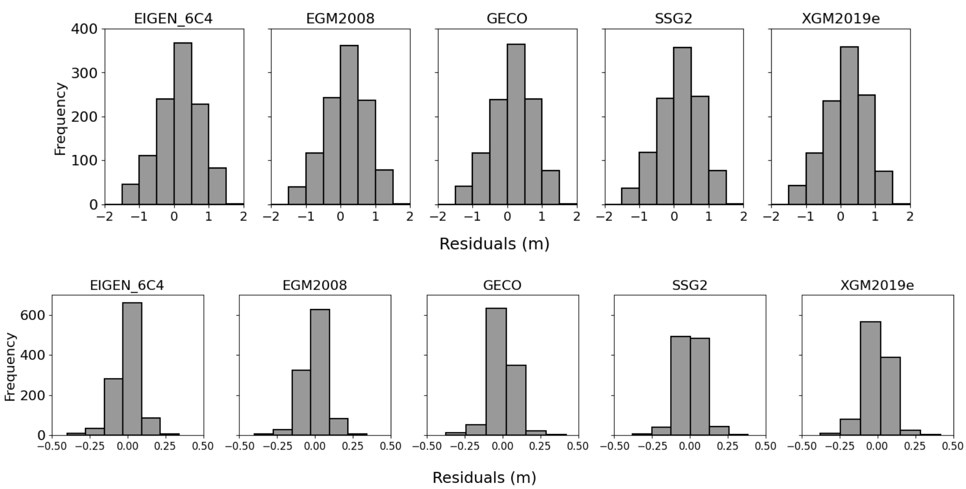

Fig. 4. Histogram of residuals before ML (up) and after MLP (down)

Table 1 summarizes the improvement in RMSE for all models achieved with the application of the machine learning techniques.

Table 1. Machine learning improvement of GGM geoid undulations

Model	GGM Best RMSE (cm)	SVR		RF		MLP	
		Best RMSE	Improvement (%)	Best RMSE	Improvement (%)	Best RMSE	Improvement (%)
SGG-UGM-2	62.93	9.44	85.00	10.81	82.82	7.73	87.72
XGM2019e_2159	62.75	9.87	84.27	10.75	82.87	8.37	86.67
GECO	63.07	9.44	85.03	10.78	82.91	7.70	87.79
EIGEN-6C4	63.09	9.61	84.77	10.80	82.88	7.96	87.38
EGM2008	63.31	9.37	85.20	10.66	83.17	7.81	87.66

In conclusion, this study shows that while increasing the degree and order of GGMs improves resolution, it can introduce high-frequency noise that may decrease accuracy. For example, at a maximum degree of 2190, RMSE values for SGG-UGM-2 increased by 9.46 cm for SVR, 11.28 cm for RF, and 7.78 cm for MLP, indicating that the optimal truncation degree varies by model. The research highlights the effectiveness of machine learning, especially the Multilayer Perceptron, in enhancing geoid undulation predictions. By combining traditional geodetic methods with data-driven approaches, this study provides a solid framework for improving GGM accuracy. Future work should include more gravity, altimetry, and GNSS data to further enhance GGM-based geoid models.

References

[1] Li, X.; Götze, H.-J. Ellipsoid, Geoid, Gravity, Geodesy, and Geophysics (Vol. 66, Pg 1660, 2001). *Geophysics* **2002**, *67*(3), 997.

[2] National Geodetic Survey. GPS on Bench Marks [Online]. **2024**. https://www.ngs.noaa.gov/GPSonBM/ (accessed Sept 9, 2024).

[3] Ince, E. S.; Barthelmes, F.; Reißland, S.; Elger, K.; Förste, C.; Flechtner, F.; Schuh, H. ICGEM – 15 Years of Successful Collection and Distribution of Global Gravitational Models, Associated Services and Future Plans. *Earth Syst. Sci. Data.* **2019**, *11*, 647–674. https://doi.org/10.5194/essd-11-647-2019.

[4] Kaloop, M. R.; Samui, P.; Rabah, M.; Al-Ajami, H.; Hu, J. W.; Zaki, A. Improving Accuracy of Local Geoid Model Using Machine Learning Approaches and Residuals of GPS/Levelling Geoid Height. *Surv. Rev.* **2022**, *54*(387), 505–518.

SPECTRAL AND MULTIVARIATE STATISTICAL ANALYSIS OF ASTROGEODETIC QUANTITIES DERIVED FROM GGM

Ahmed Abdalla

Department of Civil and Environmental Engineering, Louisiana State University, LA 70803, Baton Rouge, USA
email: aabdalla1@lsu.edu

Accurate determination of the deflection of the vertical (DoV) is essential for high-precision geoid modeling and for establishing consistent height systems [1]. In this study, we evaluate the agreement between observed DoV values obtained by the digital zenith camera and those computed from several Global Geopotential Models (GGMs) obtained from the ICGEM repository [2], including EGM2008, EIGEN_6C4, EIGEN_6C3stat, GECO, XGM2019e, and SGG_UGM_2. The comparison focuses on the north–south (η) and east–west (ξ) components of the DoV across a spherical harmonic degree/order (d/o) range truncated at 1500, with an emphasis on identifying the models and spectral ranges that best represent the measured signal.

The analysis begins with the computation of residual standard deviations (STDs) between measured and GGM-derived DoV components (Figure 1). These results reveal that EGM2008 and GECO consistently exhibit the lowest residual STDs across much of the mid-frequency domain, particularly between d/o 300 and 800. These findings indicate superior agreement with the observed DoV within this spectral range. EIGEN_6C4 demonstrates comparable performance but with slightly elevated residuals at higher degrees. In contrast, models such as XGM2019e show increased variability in the residuals at finer spatial scales, potentially reflecting differences in regularization strategies, satellite-only content, or resolution limitations in the model construction.

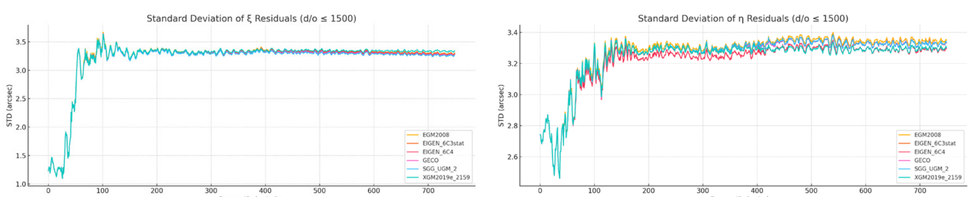

Fig. 1. Standard Deviation of residuals for ξξη

To gain further insight into model-specific residual behavior, dimensionality reduction was performed using Principal Component Analysis (PCA). PCA projections of the truncated STD vectors reveal distinct clustering patterns. Notably, EIGEN_6C4 and GECO occupy a similar region of the principal component space, suggesting shared spectral characteristics in their error structures (Figure 2.a). Conversely, XGM2019e projects further from the cluster center, reflecting its relatively distinct variance structure, particularly in the ξ component [3]. Frequency-domain analysis was also employed to examine the distribution of residual energy. Discrete Fourier Transform (DFT) plots (see Figure 2.b show that the majority of residual variance is concentrated in the low-frequency range, consistent with large-scale geophysical signal content [4]. However, model-specific distinctions emerge in the mid-frequency domain. For instance, GECO and EGM2008 exhibit smooth spectral decay, indicative of well-controlled residuals. In contrast, SGG_UGM_2 and XGM2019e display elevated spectral amplitudes in the mid- and high-frequency bands, suggesting the presence of spatially correlated errors or insufficient attenuation of high-frequency noise.

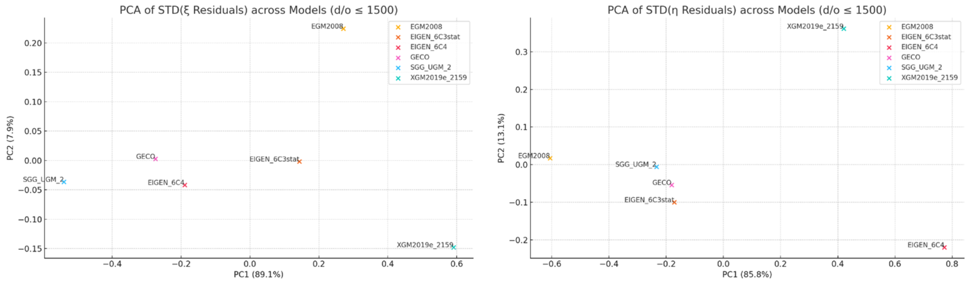

Fig. 2.a. PCA of Standard Deviation of residuals of ξ and η

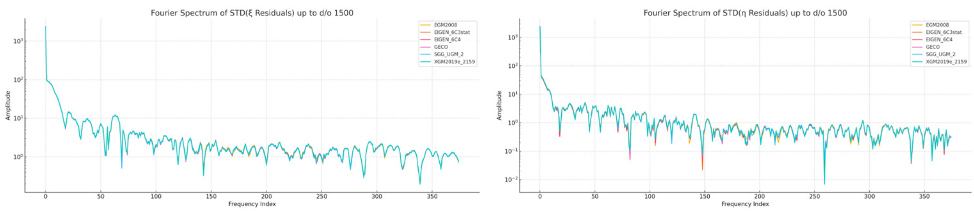

Figure 2.b. PSD of Standard Deviation of residuals of ξ and η

Complementing the DFT, power spectral density (PSD) analysis quantifies the distribution of residual energy across continuous frequency bands. The PSD plots in Figure 3 reaffirm that EGM2008 and GECO maintain consistent energy levels with minimal high-frequency amplification, whereas the other models show less spectral smoothness. These differences may be linked to the inclusion of high-resolution terrestrial data or filtering techniques employed during model development [5].

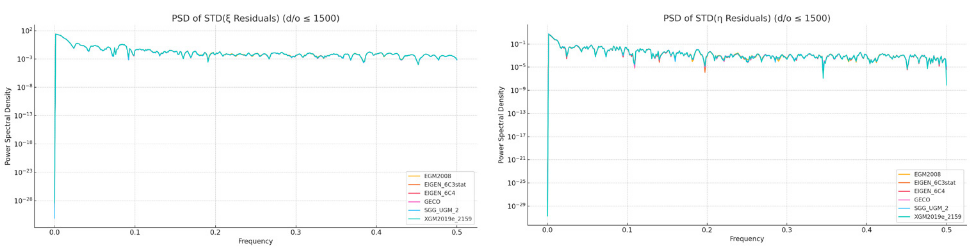

Fig. 3. PSD analysis of the residuals

Together, these multi-level analyses demonstrate that while direct residual statistics provide a baseline evaluation of GGM performance, advanced spectral and multivariate techniques offer enhanced diagnostic power. The combination of PCA, DFT, and PSD reveals model behaviors that would not be evident from spatial-domain analysis alone. Notably, the mid-degree range (d/o 300–800) emerges as the zone of optimal model–observation agreement, suggesting its importance in model truncation strategies for regional geoid applications [6].

This work highlights the value of integrating spectral and statistical methods in the evaluation of global gravity field models, particularly when validated against high-quality terrestrial observations. Such comprehensive assessments are critical for advancing geodetic infrastructure, refining geoid estimates, and ensuring robust integration of GNSS and leveling data in national height systems.

References

[1] Torge, W., & Müller, J. *Geodesy*. Walter de Gruyter. **2012**.

[2] International Centre for Global Earth Models (ICGEM), https://icgem.gfz-potsdam.de.

[3] Jolliffe, I. T., & Cadima, J. Principal component analysis: a review and recent developments. P*hilosophical Transactions of the Royal Society A*. **2016**, *374*(2065).

[4] Anderson, T. W. *The Statistical Analysis of Time Series*. Wiley. **1971**.

[5] Sneeuw, N. A semi-analytical approach to gravity field analysis from satellite observations. Deutsche Geodätische Kommission, Reihe C, Heft Nr. 527. **2000**.

[6] Sansò, F., & Sideris, M. G. (Eds.). Geoid Determination: Theory and Methods. Springer. **2013**.

REVOLUTION IN GNSS-IR AS A REMOTE SENSING TECHNIQUE FOR MONITORING SURFACE CHANGES

Mohamed Abdelhamid[1, 2], Kamil Maciuk[1]

[1] *Department of Integrated Geodesy and Cartography, AGH University of Krakow, Krakow, Poland*

[2] *Department of Civil Engineering, Helwan University, Cairo, Egypt*

E-mail: mashraf@agh.edu.pl

Global Navigation Satellite System Interferometric Reflectometry (GNSS-IR) is a powerful remote sensing technique that utilizes reflected GNSS signals to analyze environmental and anthropogenic parameters. Traditionally considered an error source in GNSS applications, multipath signals are now harnessed to extract crucial surface properties such as soil moisture, snow depth, water levels, and many other applications. This study introduces a comprehensive review of existing methodologies of GNSS-IR and its applications, discussing its role in environmental monitoring.

The methodology of GNSS-IR involves analyzing the interference patterns generated by the combination of direct and reflected GNSS signals received by ground-based antennas. This approach enables the retrieval of crucial environmental parameters by utilizing the signal-to-noise ratio (SNR) variations observed in GNSS data [1]. Research has demonstrated that extracting multipath effects from these signals provides valuable insights into surface characteristics such as soil moisture [2], water level measurements [3], detecting sea ice [4] and snow depth [5]. By leveraging geodetic GNSS receivers and specialized software tools, researchers can process these signals to estimate reflector height and other geophysical metrics with high precision.

Key applications of GNSS-IR include snow depth monitoring, where geodetic receivers and smartphones demonstrate high accuracy in measuring snow accumulation [6]. The technique is also employed in water level estimation, leveraging signal-to-noise ratio (SNR) oscillations to determine reflector height. Studies validate the effectiveness of GNSS-IR for tide gauge monitoring, achieving centimeter-level precision comparable to traditional in situ methods [7]. Recent advancements in GNSS-IR software tools have expanded its usability, integrating machine learning and cloud computing for real-time environmental monitoring [8].

Despite these advancements, challenges remain in refining GNSS-IR methodologies to account for vegetation interference, terrain variations, and atmospheric effects. Future research should focus on integrating multi-GNSS signals, improving phase center correction models, and developing adaptive algorithms to optimize reflectometry-based remote sensing. The continued expansion of GNSS constellations offers new opportunities to enhance GNSS-IR applications, ensuring its role as a cost-effective and scalable solution for environmental monitoring.

References

[1] Altuntas, C.; Tunalioglu, N. Feasibility of Retrieving Effective Reflector Height Using GNSS-IR from a Single-Frequency Android Smartphone SNR Data. *Digit. Signal Process. A Rev. J.* **2021**, *112*, 103011. https://doi.org/10.1016/j.dsp.2021.103011.

[2] Chew, C.; Small, E. E.; Larson, K. M. An Algorithm for Soil Moisture Estimation Using GPS-Interferometric Reflectometry for Bare and Vegetated Soil. *GPS Solut.* **2016**, *20*(3), 525–537. https://doi.org/10.1007/s10291-015-0462-4.

[3] Anderson, K. D. Determination of Water Level and Tides Using Interferometric Observations of GPS Signals. *J. Atmos. Ocean. Technol.* **2000**, *17*(8), 1118–1127. https://doi.org/10.1175/1520-0426(2000)017<1118:DOWLAT>2.0.CO;2.

[4] Yan, Q.; Huang, W. Sea Ice Remote Sensing Using GNSS-R: A Review. *Remote Sens.* **2019**, *11*(21). https://doi.org/10.3390/rs11212565.

[5] Chen, P.; Li, Z.; Zheng, N. A New Approach for GNSS-IR Snow Depth Monitoring with Slope Correction and Error Prediction. **2021**, 1–16. https://doi.org/10.21203/rs.3.rs-150402/v1.

[6] Pre-proofs, J.; Chen, L.; Chai, H.; Zheng, N.; Wang, M.; Xiang, M. Feasibility and Performance Evaluation of Low-Cost GNSS Devices for Sea Level Measurement Based on GNSS-IR. *Adv. Sp. Res.* **2023**. https://doi.org/10.1016/j.asr.2023.07.031.

[7] Altuntas, C.; Tunalioglu, N. A Systematic Approach for Identifying Optimal Azimuth and Elevation Angle Masks in GNSS - IR : Validation through a Sea Level Experiment. *GPS Solut.* **2023**. https://doi.org/10.1007/s10291-023-01535-0.

[8] Altuntas, C.; Tunalioglu, N. GIRAS: An Open-Source MATLAB-Based Software for GNSS-IR Analysis. *GPS Solut.* **2022**, *26*(1), 1–8. https://doi.org/10.1007/s10291-021-01201-3.

INSAR-BASED ANALYSIS OF LAND DISPLACEMENT IN SOUTHEASTERN LOUISIANA: LAKE MAUREPAS REGION

Curtis Amo Dwira, Ahmed Abdalla

Louisiana State University, Department of Civil and Environmental Engineering, Baton Rouge, Louisiana, USA
E-mail: cdwira1@lsu.edu

Land Subsidence, a vertical movement or settling of the Earth's surface is one of the geophysical concerns associated with coastal and low-lying areas particularly in the southeastern part of Louisiana where natural processes intersect with human activities such as groundwater extraction, hydrocarbon development, and infrastructure expansion [1]. This study applies an integrated approach using Interferometric Synthetic Aperture Radar (InSAR) technique specifically the Persistent Scatterer Interferometry (PSI) technique and multi-criteria analysis, specifically the Analytical Hierarchy Process (AHP), to assess surface displacement and land subsidence susceptibility in the region of Lake Maurepas between 2017 and 2020 considering ten key geospatial and environmental variables.

Lake Maurepas, which is situated between Lake Pontchartrain and the Maurepas Swamp Wildlife Management Area, is a critical zone within southeastern Louisiana. Over the years, the region has experienced increasing pressure from both natural and human processes which have led to significant land surface changes contributing to wetland loss, increased flood risk, and infrastructure instability. This study seeks to map and analyze surface deformation trends over the chosen period and identify driving factors and risk zones contributing to land subsidence to inform future mitigation and adaptation strategies [2].

To achieve the set goals, sentinel-1 radar imagery from 2017 to 2020 was used and processed using the PSI-InSAR approach to detect surface motion with a millimeter-level precision to extract vertical deformation signals from stable targets. Applying InSAR technique provides a unique advantage for regional scale monitoring due to its sensitivity to ground displacement over time. The workflow implemented in analyzing land subsidence is shown in Fig. 1.

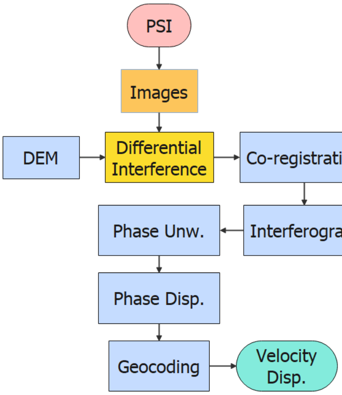

Fig. 1. PSI-InSAR data analysis procedure

The analysis provided a very complex spatial pattern of subsidence, with the most severe rates observed along the eastern and southeastern shores of Lake Maurepas. Areas with the most severe rates of land subsidence include the communities of Ruddock, Akers, and Pass Manchac, exhibiting subsidence rates ranging from –10 mm/year to –15 mm/year. These regions are characterized by unconsolidated sediments, intensive groundwater pumping, and wetland degradation, all of which contribute to accelerated land subsidence. Also, the southern and southwestern portions of the lake showed moderate deformation rates ranging between –5 mm/year and –10 mm/year. Notably, infrastructure such as Interstate 55 (I–55), which parallels the southeastern shore of the lake, intersects these zones. The presence of critical transportation corridors within subsiding regions raises significant concerns regarding the structural integrity of roads, bridges, and drainage systems, particularly under stress from hurricanes and heavy rainfall events. The northern and northwestern parts of the lake displayed relatively stable ground conditions with subsidence rates between 0 mm/year and –5 mm/year. These areas are typically known to have firmer geological substrates and low anthropogenic impact, providing a better comparison to active and vulnerable marshlands. The velocity map for the study area is shown in Fig. 2.

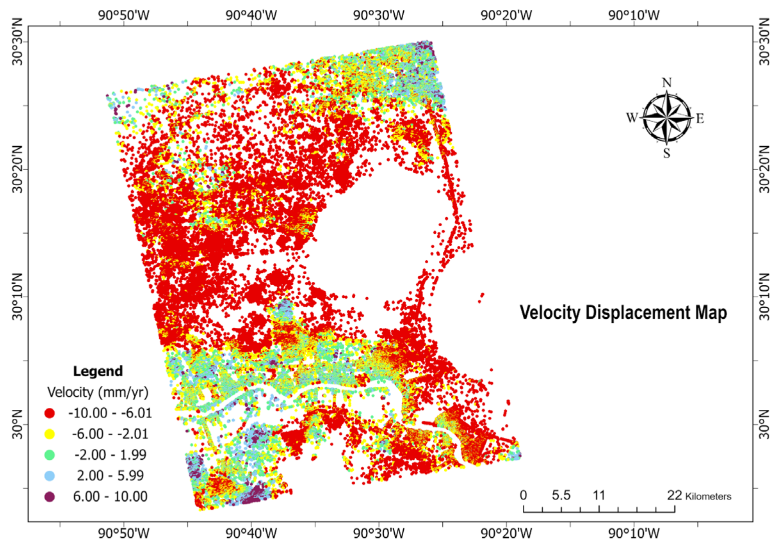

Fig. 2. Velocity Displacement Map

Decorrelation of radar signal over open water restricted coherent signal returns across the lake's central basin, but sufficient Persistent Scatterers along shorelines and wetlands provided a detailed deformation map. To clearly understand these patterns, AHP, which is one of the multi-criteria decision-making frameworks was used in this study to map subsidence susceptibility. This approach enables systematic comparison based on expert decisions by weighting factors contributing to land deformation [3]. The ten variables used for the analysis include geology, land use/land cover (LULC), aspect, slope, elevation, topographic wetness index (TWI), precipitation, distance to fault lines, distance to roads, and distance to rivers. These variables were chosen based on literature precedence and field knowledge. Pairwise comparison matrix is used to assign weight to each factor. To ensure reliability and validity of the model, consistency checks were applied to measure the coherence and transitivity of these comparisons, which indicates how logically the judgments are related. The consistency ratio (CR) for the matrix was below 0.1, indicating an acceptable level of logical consistency in the weighting process. The derived weights revealed that Geology (26.1%) and Land Use/Land Cover (13.72%) were the most influential factors contributing to subsidence. This reflects the dominance of unconsolidated Holocene sediments in the region and the impact of anthropogenic activities such as road construction, urbanization, and industrial activity. Elevation and distance to faults also carried notable weights, suggesting that both topographic setting and structural geology influence susceptibility patterns in this region. Also, moderately weighted criteria such as TWI and aspect revealed the significance of hydrological accumulation and slope orientation which facilitate soil moisture retention and promote subsidence in saturated zones. Slope and distance to rivers also played essential roles, especially in areas adjacent to natural or artificial drainage systems. Precipitation, while an important climatic driver, was assigned the lowest weight due to its indirect impact relative to more immediate geological and land-use conditions. The result for pairwise comparison is shown in Fig. 3.

Matrix		Geology 1	LULC 2	Aspect 3	TWI 4	Slope 5	Distance to Road 6	Distance to river 7	Precipitation 8	Distance to Fault 9	Elevation 10	normalized principal Eigenvector
Geology	1	1	3	4	5	5	6	5	4	1	1	26.10%
LULC	2	1/3	1	3	2	2	3	3	3	1	1	13.72%
Aspect	3	1/4	1/3	1	2	2	2	1/2	3	1	1	8.77%
TWI	4	1/5	1/2	1/2	1	2	2	2	3	1	1	8.78%
Slope	5	1/5	1/2	1/2	1/2	1	2	1/2	3	1	1	6.66%
Distance to Road	6	1/6	1/3	1/2	1/2	1/2	1	1/2	2	1	1	5.20%
Distance to river	7	1/5	1/3	2	1/2	2	2	1	2	1	1	8.22%
Precipitation	8	1/4	1/3	1/3	1/3	1/3	1/2	1/2	1	1	1	4.40%
Distance to Fault	9	1	1	1	1	1	1	1	1	1	1	9.08%
Elevation	10	1	1	1	1	1	1	1	1	1	1	9.08%

Fig. 3. A Pairwise Comparison

The weighted factors were integrated within a GIS environment to produce a subsidence susceptibility map of the Lake Maurepas region. The results were classified into five categories (Very Low, Low, Moderate, High, and Very High susceptibility). The High to Very High categories were predominantly found along the eastern and southeastern shores conforming with areas of active subsidence detected by InSAR. Low to Very Low susceptibility zones were seen in the northern and northwestern parts of the study area. These areas show more geologically stable regions with limited development and better drainage, consistent with InSAR findings showing minimal surface displacement as shown in Fig. 4. The strong spatial correlation between modeled susceptibility zones and observed subsidence patterns confirms the reliability of the integrated approach.

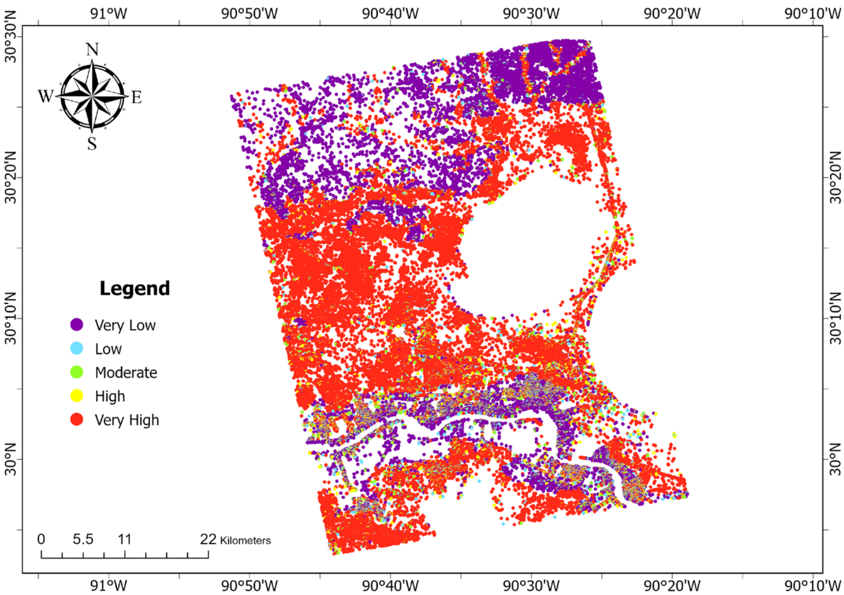

Fig. 4. Land Displacement Susceptibility Map

The findings of this study have several important implications. First, the overlap between infrastructure networks and areas of active subsidence suggests the need for long-term monitoring, maintenance prioritization, and possible design adjustments to protect critical assets like I–55. Second, the susceptibility map offers a valuable decision-support tool for land use planning, wetland conservation, and disaster preparedness. By identifying priority areas for intervention, the model supports the development of adaptive strategies to mitigate future impacts. This research also demonstrates the advantages of combining remote sensing data with structured geospatial decision models. PSI-InSAR provides highly accurate and repeatable measurements of land surface change, while AHP offers a flexible and transparent framework for evaluating complex spatial relationships. Together, they enable a comprehensive understanding of the causes and consequences of land subsidence across variable landscapes.

Nevertheless, certain limitations are acknowledged. InSAR's inability to generate reliable data over open water and dense vegetation limits its coverage in some wetland environments. AHP, while systematic, depends on expert input for pairwise comparisons, which may introduce subjectivity. Future research should explore the integration of machine learning techniques, such as Random Forest or Gradient Boosting, to assign weights more objectively and explore nonlinear relationships between variables. Additionally, incorporating ground-based data from GNSS stations could enhance the calibration and validation of the deformation model.

In conclusion, this study provides a rigorous and replicable framework for subsidence analysis in complex coastal settings. By integrating PSI-InSAR and AHP, the methods delivered a better understanding of both where and why land subsidence is occurring in the Lake Maurepas region. These insights contribute directly to ongoing efforts in coastal resilience, infrastructure planning, and environmental stewardship in southeastern Louisiana. As subsidence continues to threaten ecological systems, human settlements, and critical infrastructure, the tools and methodologies demonstrated here will be increasingly essential for guiding evidence-based decision-making and long-term sustainability planning.

References

[1] Khan, J.; Ren, X.; Hussain, M. A.; Jan, M. Q. Monitoring Land Subsidence Using PS-InSAR Technique in Rawalpindi and Islamabad, Pakistan. *Remote Sens*. **2022**, *14*, 3722. https://doi.org/10.3390/rs14153722.

[2] Shaffer, G. P.; Day, J. W.; Kandalepas, D.; Wood, W. B.; Hunter, R. G.; Lane, R. R.; Hillmann, E. R. Decline of the Maurepas Swamp, Pontchartrain Basin, Louisiana, and Approaches to Restoration. *Water*. **2016**, *8*(3), 101. https://doi.org/10.3390/w8030101.

[3] Mabrouk, B.; Barkat, L.; Achour, H.; Irfan, M.; Dewan, A. GIS-based MCDM–AHP modeling for flood susceptibility mapping: A case study of the Gadilam River Basin, Tamil Nadu, India. *Geocarto Int*. **2022**, *37*(3), 827–849. https://doi.org/10.1080/10106049.2020.1768596.

INTEGRATING INSAR AND MACHINE LEARNING FOR LAND SUBSIDENCE DETECTION AND PREDICTION IN THE CAPITAL AREA OF LOUISIANA

Desmond Kangah and Ahmed Abdalla

Louisiana State University, Civil and Environmental Department Baton Rouge, Louisiana, USA
E-mail: dkanga1@lsu.edu

The increasing frequency and severity of geohazards such as land deformation is closely linked to both human and natural activities. These phenomena pose significant threats to infrastructure, ecosystems, and human safety [5]. As urban expansion and climate variability accelerate, the need for accurate detection and prediction of ground deformation becomes more critical for effective risk mitigation, informed land-use planning, and the development of sustainable infrastructure [2]. In this context, remote sensing technologies, particularly Interferometric Synthetic Aperture Radar (InSAR), have emerged as valuable tools for observing surface displacements over time [4].

This study focuses on the capital region of Louisiana, an area characterized by complex geological structures, substantial hydrological activity, and significant anthropogenic modifications. The integration of InSAR techniques with advanced machine learning (ML) models was undertaken to both detect and predict land subsidence across the region. The synergy between Earth observation data and ML provides a powerful means of understanding spatial patterns of deformation and forecasting potential high-risk zones [9].

InSAR enables the precise measurement of ground displacement at the millimeter scale by analyzing phase differences in radar signals acquired by satellites over time. For this study, Sentinel-1 Synthetic Aperture Radar (SAR) data were used due to their high spatial resolution, open access, and consistent temporal coverage [10]. A time-series analysis was performed on the SAR data to derive ground deformation velocities across the study area. These velocities were then used as the target variable for predictive modeling shown in Figure 1.

To model the spatial variability of subsidence, ten predictor variables were selected based on their relevance to geological and environmental processes. This included geology, distance from known fault lines, distance from major rivers, proximity to road networks, precipitation levels, land use/land cover (LULC) classifications, digital elevation model (DEM) values, slope, aspect, and the topographic wetness index (TWI). Each of these features has a known or hypothesized influence on land stability and subsidence behavior [7, 12].

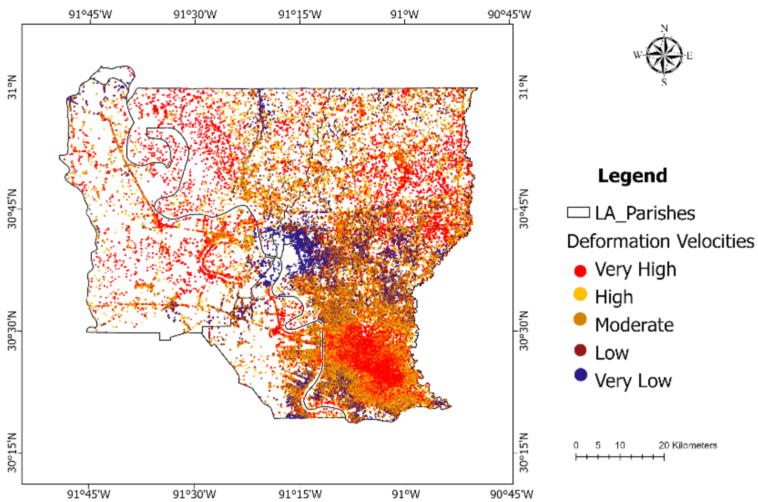

Fig. 1. PSI Calculated deformation velocities of subsidence

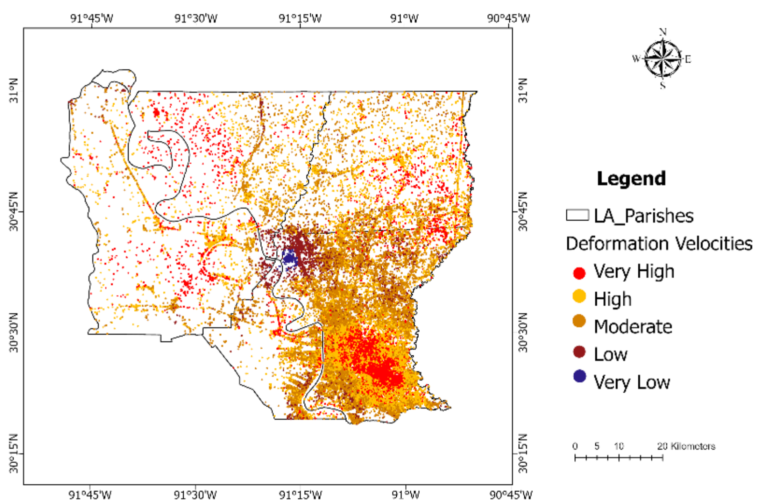

Fig. 2. Random Forest Calculated deformation velocities of subsidence

Three ensemble ML algorithms were employed for predictive modeling: Random Forest (RF), eXtreme Gradient Boosting (XGBoost), and Light Gradient Boosting Machine (LightGBM). These models are well-suited to handle non-linear relationships and interactions between input variables, and they are robust against overfitting, particularly in geospatial applications [1, 3, 6]. Among the models tested, the Random Forest model exhibited superior performance, achieving a coefficient of determination (R^2) score of 0.903. This high level of predictive accuracy suggests that the RF model was effective in capturing the complex interactions among the environmental and geological predictors. The results generated from the Random Forest model are illustrated in Figure 2, which displays the predicted ground deformation, while Figure 1 presents the mapped extent of subsidence-prone zones, providing a visual summary of the model's outputs.

To further interpret the model and understand the relative contribution of each predictor variable, a feature importance analysis was conducted using the Mean Decrease in Gini index shown in Figure 3. This method ranks features based on their impact on reducing uncertainty in the decision-making process of the model. Geology emerged as the most significant factor influencing subsidence, followed by proximity to fault lines and precipitation. These findings are consistent with known mechanisms of ground deformation, as geological formations determine soil compressibility and strength, faults introduce structural weaknesses, and precipitation influences soil saturation and compaction [11, 12]. Conversely, land use/land cover was found to make the least contribution to the model's predictions, indicating that anthropogenic surface cover types may not directly correlate with subsidence rates in this region.

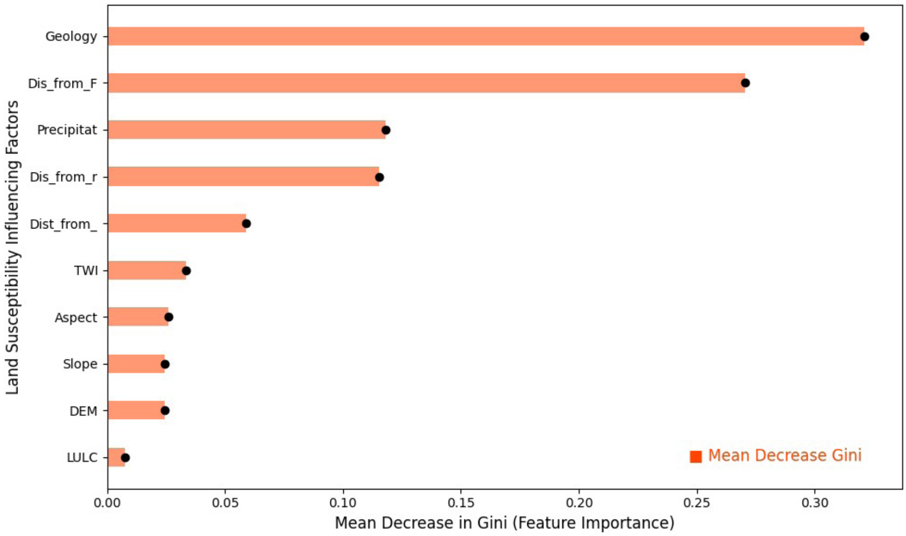

Fig. 3. Feature Importance using Mean Decrease Gini

The XGBoost and LightGBM models, while still effective, yielded comparatively lower performance, with R^2 values of 0.7695 and 0.7362 respectively. The differences in accuracy among the models can be attributed to the way each algorithm handles feature interactions and data structure. While XGBoost and LightGBM are highly efficient and capable of handling large datasets, the Random Forest model's bootstrapping and averaging approach proved more suitable for this application.

To enhance model interpretability, SHAP (Shapley Additive exPlanations) values were also calculated. SHAP provides a game-theoretic approach to explain the output of ML models by assigning each feature an important value for a particular prediction [7, 8]. SHAP values offer local and global interpretability, enabling a more detailed understanding of how each feature contributes to subsidence risk at different locations. Figure 4 display the SHAP and Mean Decrease Gini values, offering complementary perspectives on feature influence.

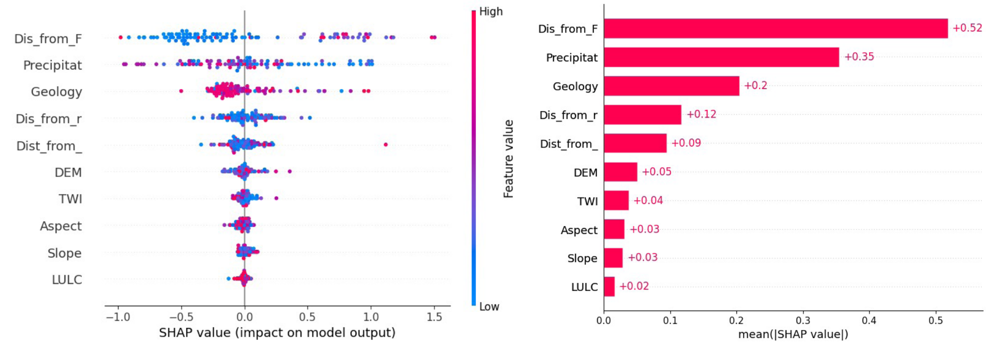

Fig. 4. Parameters interpretation by SHAP

The combined use of InSAR data and ML not only improves the accuracy of ground deformation detection but also supports the development of early warning systems and strategic land management practices [12]. The methodology presented in this study represents a robust and scalable framework for intelligent geohazard assessment, with significant potential for application in other urban and peri-urban areas experiencing subsidence or landslide risks.

In conclusion, the integration of satellite-based InSAR data with ensemble machine learning techniques provides a powerful approach for monitoring and predicting land subsidence. The insights gained through this study emphasize the critical role of geological and hydrological variables in driving subsidence processes. Furthermore, the application of explainable AI tools enhances trust and transparency in model outcomes, making the results more actionable for policymakers, urban planners, and disaster management authorities. This research underscores the importance of leveraging cutting-edge technologies to address complex environmental challenges in a data-driven and proactive manner.

References

[1] Breiman, L. Random forests. *Machine learning*. **2001**, *45*, 5–32.

[2] Chaussard, E.; Wdowinski, S.; Cabral-Cano, E., and Amelung, F. Land subsidence in central Mexico detected by ALOS InSAR time-series. *Remote Sensing of Environment*. **2017**, *140*, 94–106.

[3] Chen, T., and Guestrin, C. XGBoost: A scalable tree boosting system. *Proceedings of the 22nd ACM SIGKDD*; **2016**, 785–794.

[4] Ferretti, A.; Prati, C., and Rocca, F. Permanent scatterers in SAR interferometry. *IEEE Transactions on Geoscience and Remote Sensing*. **2001**, *39*, 8–20.

[5] Guzzetti, F.; Reichenbach, P.; Cardinali, M.; Galli, M., and Ardizzone, F. Landslide hazard assessment in the Staffora basin, northern Italian Apennines. *Geomorphology*. **2005**, *72*(1–4), 272–299.

[6] Ke, G.; Meng, Q.; Finley, T.; Wang, T.; Chen, W.; Ma, W., and Liu, T. Y. LightGBM: A highly efficient gradient boosting decision tree. *Advances in Neural Information Processing Systems*. **2017**, 30.

[7] Lee, S.; H. J., and Choi, J. Application of remote sensing data and GIS-based logistic regression model for landslide susceptibility mapping. *Remote Sensing*. **2020**, *12*(6), 1049.

[8] Lundberg, S. M., and Lee, S. I. A unified approach to interpreting model predictions. *Advances in Neural Information Processing Systems*. **2017**, 30.

[9] Pham, B. T.; Bui, D. T.; Prakash, I.; Dholakia, M. B., and Le, H. V. Machine learning models for landslide susceptibility mapping. *Geoscience Frontiers*. **2021**, *12*(2), 543–562.

[10] Torres, R.; Snoeij, P.; Geudtner, D.; Bibby, D.; Davidson, M.; Attema, E., and Rosich, B. GMES Sentinel-1 mission. *Remote Sensing of Environment*. **2012**, *120*, 9–24.

[11] Wang, J.; Gao, X.; Liu, Y., and Tang, C. Mapping land subsidence in Beijing using Sentinel-1 data and PS-InSAR technique. *Remote Sensing*. **2020**, *12*(7), 1144.
[12] Zhou, W.; Sun, Q., and Zhang, L. Spatio-temporal analysis of land subsidence using InSAR time series and geospatial data in the Yangtze River Delta, China. *Remote Sensing*; **2020**, *11*(13), 1541.